Heliyon 10 (2024) e35061

Contents lists available at ScienceDirect

Heliyon

journal homepage: www.cell.com/heliyon

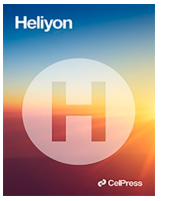

Research article

A comprehensive study on electron and hole transport layers for designing and optimizing the efficiency of $MoSe_2$-Based solar cells using numerical simulation techniques

Avijit Ghosh [a,*], Abeer A. Hassan [b], H.A. Alrafai [b], Siham Khalaf Alla Abdelrahim [b]

[a] Department of Electrical and Electronic Engineering, Begum Rokeya University, Rangpur, 5400, Bangladesh
[b] Department of Chemistry, Faculty of Science, King Khalid University, PO Box 9004, Abha, 61413, Saudi Arabia

ARTICLE INFO

Keywords:
$MoSe_2$
HTL
SnS_2
Efficiency
SCAPS-1D

ABSTRACT

Researchers have recently shown a great deal of interest in molybdenum diselenide ($MoSe_2$)-based solar cells due to their outstanding semiconducting characteristics. However, discrepancies in the band arrangement at the $MoSe_2$/ETL (electron transport layer) and hole transport layer (HTL)/$MoSe_2$ interfaces impede performances. In this research, a device combination with Ag/FTO/ETL/$MoSe_2$/HTL/Ni is employed, where 7 HTLs and 3 different ETLs have been utilized to explore which device arrangement is superior. To achieve the most effective device arrangement, the effects of various device variables, such as thickness, donor density, acceptor density, defect density, temperature, series, and shunt resistance, are optimized. The computational evaluation under AM 1.5 light spectrums (100 mW/cm^2) is performed using the SCAPS-1D simulator. When the several device parameters were optimized, the device that was correlated with Ag/FTO/SnS_2/$MoSe_2$/V_2O_5/Ni revealed the highest overall performances among the three different ETL (In_2S_3, SnS_2, ZnSe)-based devices, with measuring a PCE of 34.07 %, a V_{OC} of 0.918 V, a J_{SC} of 42.565 mAcm^{-2}, and an FF of 87.19 %. This recommended $MoSe_2$-based solar cell exhibits outstanding efficiency in terms of maintenance and comparison to numerical thin film solar cells, highlighting $MoSe_2$ as an attractive option for solar energy systems while eliminating toxicity challenges.

1. Introduction

Globally, there is an ever-increasing demand for energy. Since there are no specialized energy storage technologies available, the supply of acceptable energy sources is steadily declining. This means that a clean energy source is needed that is long-term, renewable, affordable, and environmentally benign. Solar energy is one option in this regard. Solar cells are a great option because they minimize the demand for fossil fuels and lower the cost of power generation [1–3]. However, single-junction solar cells are unable to achieve their theoretical efficiency limit, also referred to as the Shockley-Queasier limit, due to the intrinsic bandgap of absorber materials. The reliance on solar energy is increasing thanks to recent advancements in research. The dependence on solar energy is on the rise, driven by innovations aimed at enhancing its efficiency. In our country, various government electrification programs emphasize the importance of solar power [4]. Energy is one of the most crucial factors for the advancement and prosperity of any nation. When considering sustainable energy, it is essential to replace existing sources with renewable energy supplies. The continuous use of fossil

* Corresponding author.
E-mail address: avijitghosheee@gmail.com (A. Ghosh).

https://doi.org/10.1016/j.heliyon.2024.e35061
Received 26 June 2024; Received in revised form 12 July 2024; Accepted 22 July 2024
Available online 24 July 2024

fuels has already caused several problems, including pollution, health issues, and global warming [5]. Therefore, with the pressing demand for energy and growing environmental apprehensions, researchers are directing their efforts towards alternative sources such as solar energy, which can fulfil our energy requirements without causing harm to the environment [6]. Polycrystalline silicon photovoltaic solar cells dominate the global market and account for more than 90 % of PV production [7,8]. Si solar structure's large production cost and poor efficiency are its disadvantages. The maximum power conversion efficiency for crystalline and polycrystalline Si-based photovoltaic cells was observed at 26.7 % and 24.4 %, respectively [9]. These days, scientists are focusing on producing extremely efficient thin-film solar cells (TFSCs) using materials that are readily available, safe, and appropriate for the environment [10]. Inorganic perovskites, which might prove extremely useful as solar cell absorber materials, have also been the subject of research lately [11–15].

Molybdenum diselenide ($MoSe_2$) is one of the most promising and effective absorber materials among TFSCs due to its stability, affordability, and lack of toxicity. This substance is a transitional metallic dichalcogenide (TMD). Numerous research groups have thoroughly examined the diverse electrical, optical, catalytic, and magnetic properties of TMD materials [16–18]. Among its benefits are its inexpensiveness, ease of manufacture, excellent PCE, and broad-spectrum responses [19]. They have the generic formula MX_2, where X represents a chalcogen (S, Se, and Te) and M denotes a transition metal (Mo, W, Nb, and Ti). TMD compounds are being studied as absorbers along with transport layers because of their appropriate structural and electronic characteristics [20]. $MoSe_2$ exhibits a 10^{-3} Sm^{-1} electrical conductivity [21], and it has a light absorption coefficient between 10^4 and 10^6 cm^{-1} [22]. The bandgap of this absorber can be adjusted based on a number of variables, including thickness, temperature, and doping. Because of these advantageous qualities, $MoSe_2$ is a strong contender for photovoltaic applications. The usefulness of $MoSe_2$-based technologies has been shown in the past conceptually [23–25] and practically works [26,27]. The initial $MoSe_2$-based SC was created experimentally early in 1991 by Jager-Waldau et al., and with their n-ZnO/p-$MoSe_2$/Au single junction technology, they were able to attain a PCE of 0.12 % below 70 mW/cm^2 of light [26]. In a study conducted in 2016, a comparatively narrow absorber (1.5 μm) was used to create $MoSe_2$/GaN heterojunction SC, which was discovered to have 1.29 % PCE [27]. Counter electrodes (CEs), hole transport layers (HTL), and electron transport layers (ETL) have all been used by researchers over the past few years to improve the efficiency of solar energy [10,28]. Although the simulation study may offer a very effective SC model, these structures' consistency and endurance create problems in practical applications. The efficiency is permanently decreased by temperature and environmental deterioration.

A substance called an ETL layer is placed in between a SC's absorber and window layers. Another name for it is the buffer layer. Among its functions are transferring the electrons produced by photosynthesis to the electrode, decreasing flaws, enhancing band alignment, and shielding the absorber from corrosion and harm. Examples include ZnS, ZnSe, SnS_2, ZnO, In_2S_3, TiO_2, and CdS as ETL. Due to their excellent band gap alignment, high transparency in the visible range, and simple fabrication technique, In_2S_3, and SnS_2 are frequently employed as ETL layers [29–31]. Conversely, a p + -type substance called a hole transport layer (HTL) is applied to a SC's back surface. Concerning PV effectiveness, the HTL layer offers a number of advantages. An HTL layer stops the surface recombination by generating an electric field at the contact with the p-type absorber. In addition, it can improve the ohmic contact between the back electrode and function as a light reflector [32]. HTL layers can be found in V_2O_5, SnSe, MoS_2, GeSe, MoO_3, GaAs, and PTAA, to name a few [33,34]. Among them, V_2O_5 has a direct band gap of around 2.20 eV together with good thermal stability, optical absorption coefficient, and long-term performance, and it has just been added to the high priority production list due to its minimal environmental impact and inexpensive fabrication techniques [10].

In this computational study, the SCAPS-1D software is used to examine seven distinct arrangements of HTL, with $MoSe_2$, SnS_2, nickel (Ni), and silver (Ag) being used as the absorber layer, ETL, back, and front contacts, respectively. Once an exceptionally effective HTL has been optimized, three ETLs (In_2S_3, SnS_2, and ZnSe) are combined and subsequently modified utilizing a device structure of Ag/FTO/ETL/$MoSe_2$/V_2O_5/Ni. Furthermore, after optimizing absorber layer thickness, ETL thickness, absorber layer defect density, and HTL acceptor and defect density, the impacts of temperature, generation, recombination, j-v features, and quantum efficiency are noted. Ultimately, based on the combined effectiveness of the three configurations under investigation, the ideal device for the study was chosen. All things considered, the results of this numerical research are essential for creating environmentally safe solar cells made of $MoSe_2$ absorber material. The whole work has been completed by using the Advanced Energy Materials and Solar Cell Research Laboratory, Department of Electrical and Electronic Engineering, Begum Rokeya University, Rangpur, 5400, Bangladesh.

2. Simulation techniques with device structures and band alignments

2.1. Simulation techniques

SCAPS-1D, a computational simulation tool created by Professor Marc Burgelman (version 3.3.07), was used in this study [35]. SCAPS-1D was selected as the simulator for our solar device due to its advantages over other software options and its consistent agreement with findings from prior research [36,37]. In the context of SCAPS-1D simulations of solar cells, originality contributes in a variety of ways. These include novel designs, novel material properties, sophisticated modelling methods, optimization studies, integration with experimental data, performance analysis, investigation of novel phenomena, comparative studies, and instructional materials. All of these factors have the potential to greatly progress our knowledge and lead to the creation of solar cells that are more affordable and efficient. Solving 1-D semiconductor equations, including the well-known transport equation, continuity equation, and Poisson's equation, and taking into consideration one or more recombination mechanisms are essential steps towards understanding the fundamental physics of SCAPS. The charge carrier (electrons and holes) flow inside a solar cell is described by the transport equation, while the continuity equation links the processes of carrier formation, recombination, and transport. Poisson's formula clarifies the distribution of electrostatic potential in the solar cell by taking into account the electric field and charge distribution.

"Diffusion length" denotes the distance over which diffusion substantially affects carrier mobility in a solar cell, whereas "diffusivity" describes the capacity of charge carriers to disperse inside a material. In the context of solar cells, carrier lifetime refers to the mean amount of time that a charge carrier—an electron or a hole—remains in a material before recombining or disappearing. Open-circuit voltage is the voltage across a solar cell's terminals when there is no external load. Through the solution of equations (1)–(3), which establish the structure, SCAPS may calculate multiple performance measures for photovoltaic (PV) devices [38,39].

$$\frac{\partial^2 \phi}{\partial^2 x} = -\frac{q}{\varepsilon_r \varepsilon_0}\left(p - n + N_D - N_A + p_t - n_t\right) \tag{1}$$

$$\frac{1}{q}\frac{\partial J_p}{\partial x} - R_p + G_p = 0 \tag{2}$$

$$\frac{1}{q}\frac{\partial J_n}{\partial x} - R_n + G_n = 0 \tag{3}$$

In the equation provided, the terms represent the following:

ε_o permittivity in free space, q elementary charge, ϕ electrostatic potential, the relative permittivity is denoted by (ε_r), (N_A, N_D) acceptor and donor density, respectively, (n, p) electron and hole concentrations, respectively, (G_n, G_p) generation frequency of electrons and holes, (n_t, p_t) trapped electron and hole concentrations, respectively, (J_n, J_p) electron and hole density currents, respectively, (R_n, R_p) recombination rates of electrons and holes, respectively. Equations (4) and (5) define (J_p, J_n), respectively.

$$J_n = q\mu_n n\frac{\partial \phi}{\partial x} + q D_n \frac{\partial n}{\partial x} \tag{4}$$

$$J_p = q\mu_p p\frac{\partial \phi}{\partial x} - q D_p \frac{\partial p}{\partial x} \tag{5}$$

Where μ_p and μ_n denote the mobility of holes and electrons, respectively, and D_n and D_p represent the diffusion coefficient of electron and hole. Additionally, the mathematical formula for the absorption rate utilized in the analyses is described as [40]:

$$\alpha(h\upsilon) = B\alpha\sqrt{h\upsilon - E_g} \tag{6}$$

In this context, Bα denotes a constant coefficient defined as 10^5 cm^{-1} $eV^{-0.5}$ and hυ signifies the photon energy.

2.2. Structure of the devices and band alignments

This study examines a $MoSe_2$-based n-i-p structured heterojunction SC (solar cell), as shown in Fig. 1(a), where the n, i, and p regions stand for the active layer, HTL, and ETL, respectively. A computational investigation is carried out using three distinct ETLs (In_2S_3, SnS_2, and ZnSe) and seven separate HTLs (V_2O_5, SnSe, MoS_2, GeSe, MoO_3, GaAs, and PTAA) inside the device structure, which consists of the right contact, FTO, ETL, absorber layer, HTL, and left contact. The $MoSe_2$ material acts as an absorber layer and is often positioned between the ETL and the HTL. Light illuminating this layer causes excitons to arise. The ETL functions as a hole-blocking layer when excitons come into contact with the ETL/active layer, preventing the hole from passing through the ETL and permitting the electron to proceed. Similar behaviors are shown by the HTL/absorber layer, which blocks electrons and makes it easier for holes to flow through. Here, an intrinsic electric field is vital because it facilitates the dissociation of excitons. Fig. 1(b) shows the band alignments of the Ag/FTO/ETL/$MoSe_2$/HTL/Ni structures. The work function of nickel (Ni) used in various previous research papers is

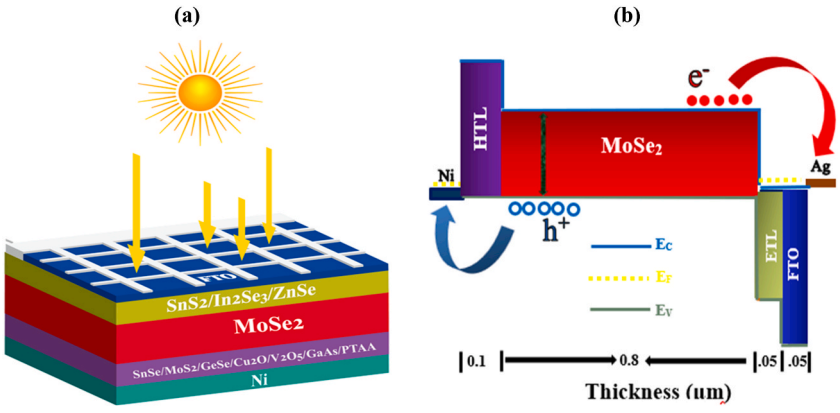

Fig. 1. (a) Schematic design and (b) band alignments of Ag/FTO/ETL/$MoSe_2$/HTL/Ni PV cell.

higher than 5 eV [41,42]. In Ag/FTO/ETL(In_2S_3,SnS_2,ZnSe)/$MoSe_2$/V_2O_5/Ni solar cell structures, the high work function of Ni forms an effective Schottky barrier for electron collection and aligns well with the valence band of V_2O_5 for efficient hole transport. This reduces recombination losses, ensures good electrical conductivity, and enhances the overall efficiency and stability of the solar cell [43].

While data from literary sources was used to optimize the other layer characteristics, simulation was used to optimize the thickness, defect, and doping concentrations of the absorber layer. In this setup, a perfect tunnel free of optical loss and electrical resistance connects the absorber and HTL. Optimizing the thickness of Ag/FTO/ETL(In_2S_3,SnS_2,ZnSe)/$MoSe_2$/V_2O_5/Ni solar cells using the quarter-wavelength principle enhances light absorption and minimizes reflection. The principle states that if a layer's thickness is an odd multiple of λ/4 (where λ is the wavelength of light within the medium), destructive interference will reduce reflected light, increasing transmission and absorption. For the FTO layer, optimizing thickness to λ/4 for relevant wavelengths (500–700 nm) enhances transparency and light entry. Similarly, In_2S_3, SnS_2, ZnSe, and $MoSe_2$ layers should be λ/4 thick to maximize light absorption by reducing reflection. The V_2O_5 layer also benefits from this principle to ensure optimal light transmission and minimal reflection. Calculating the thickness involves $d = \frac{\lambda}{4n}$ (where n is the refractive index), but practical fabrication constraints must be considered.

In order to prevent shunting and shield the upper layers from sputtering damage and solvent exposure, this arrangement incorporates a conformal recombination layer in between the absorber layers. While Table 2 displays all of the input values for all of the HTL materials, Table 1 provides all of the electrical parameters used in the simulations, which were derived from pertinent computational and experimental research published in the literature for absorber and ETL materials. Parameters such as layer thickness (t), relative dielectric constant (ε_r), electron affinity (χ), electron and hole mobility (μ_n & μ_h), bandgap (E_g), donor and acceptor densities (N_D & N_A), valence band and conduction band effective state densities (N_v & N_c), and total defect concentration (N_t) are included. Additionally, Table 3 presents the interface characteristics of the In_2S_3/$MoSe_2$, SnS_2/$MoSe_2$, ZnSe/$MoSe_2$, and $MoSe_2$/V_2O_5 systems, enabling examination of the effect of defect concentration while maintaining a consistent overall defect density at the interface.

3. Result and discussion

3.1. HTL optimization

A mixture of one ETL material and seven HTL materials is used to examine the optimal HTL material; the $MoSe_2$ material, rear, and front contacts remain fixed during the entire process, as shown in Fig. 2. The obtained data indicates that the device structure with Ag/FTO/SnS_2/$MoSe_2$/V_2O_5/Ni performs relatively better, where the power conversion efficiency (PCE), fill factor (FF), short circuit current density (J_{SC}), and open circuit current voltage (V_{OC}) are, respectively, 34.07 %, 87.19 %, 42.565 mAcm^{-2}, and 0.918 V. While MoS_2, GeSe, MoO_3, GaAs, and PTAA are examples of other HTL materials that show efficiency at or over 30–33 %, SnSe performs noticeably worse, with a PCE of 28.41 %, a V_{OC} of 0.793 V, a J_{SC} of 42.419 mAcm^{-2}, and an FF of 84.43 %. The reduced hole mobility along with the poor band alignment of SnSe are the reasons for this inferior performance. The photovoltaic effect determines a solar cell's I–V properties. Photons from the sun's rays are absorbed by the semiconductor material in the cell, forming electron-hole pairs. At the p-n junction, an electric field separates these charge carriers, creating a current. While the material qualities and the cell's working circumstances have an impact on the output voltage (V), the output current (I) is determined by the intensity of the light. Generally speaking, the I–V curve exhibits a current that falls as the voltage rises and a maximum power point when the voltage multiplied by the current is at its highest. Simulations with constant thickness, bandgap, donor density, acceptor density, and defect density for the absorber layer were run in order to determine the best combination of ETL and HTL. Since V_2O_5 performed better than other HTLs, it was chosen as the HTL for additional simulation as well as numerical evaluation. Table-4 shows the all output values of Ag/FTO/SnS_2/$MoSe_2$/V_2O_5/Ni structures with seven different HTL materials.

3.2. Variations in the defect and doping density of the HTL layer along with their impact on PV parameters

The appropriate HTL layer can facilitate the correct conveyance and collection of photogenerated holes while obstructing the flow of electrons (the minority carrier). It consequently lessens carrier recombination. Demonstrating the impact of the HTL layer on SC

Table 1
SCAPS-1D Simulation parameters for absorber, ETLs, and FTO layers.

Parameters	$MoSe_2$ [44]	ZnSe [45]	In_2S_3 [46]	SnS_2 [47]	FTO [48]
Layer thickness, t (nm)	0.8	50	50	50	50
Band gap, E_g (eV)	1.10	2.70	2.1	2.240	3.6
Electron affinity, χ (eV)	4.372	4.09	4.65	4.240	4.5
Dielectric permittivity (relative), ϵ_r	13.60	10.0	13.5	10.0	10
Hole mobility, μ_h (cm^2/(Vs))	25	20	210	50	20
Electron mobility, μ_n (cm^2/(Vs))	100	50	400	50	100
VB effective density of states, N_V (cm^{-3})	1.8×10^{19}	1.8×10^{19}	4×10^{13}	1.8×10^{19}	1.8×10^{19}
CB effective density of states, N_C (cm^{-3})	2.2×10^{18}	2.4×10^{18}	1.8×10^{19}	2.2×10^{18}	2×10^{18}
Defect density, N_t (cm^{-3})	1×10^{13}	1×10^{14}	1×10^{14}	1×10^{14}	1×10^{14}
Shallow uniform acceptor density, N_A (cm^{-3})	1×10^{18}	0	0	0	0
Shallow uniform donor density, N_D (cm^{-3})	0	1×10^{17}	1×10^{17}	1×10^{17}	1×10^{18}

Table 2
SCAPS-1D Simulation parameters for HTL layers.

Parameters	V_2O_5 [10]	SnSe [49]	MoS_2 [50]	GeSe [51]	MoO_3 [34]	GaAs [34]	PTAA [34]
t(nm)	100	100	100	100	100	100	100
E_g *(eV)*	2.20	1.2	1.23	1.41	3.0	1.42	2.96
χ (eV)	3.40	4.2	4.2	4.07	2.3	4.07	2.30
ε_r	8.0	10.0	4.0	14.30	18.0	12.90	9.0
N_C (cm^{-3})	9.2×10^{19}	2.8×10^{18}	7.5×10^{17}	4×10^{18}	1×10^{19}	2.2×10^{18}	2×10^{21}
N_V (cm^{-3})	5×10^{20}	4.75×10^{18}	1.8×10^{18}	1.75×10^{19}	2.2×10^{18}	1.8×10^{19}	2×10^{21}
$\mu_n(cm^2/(Vs))$	150	130	100	17	210	8500	1
$\mu_h(cm^2/(Vs))$	100	56.1	150	17	210	400	40
N_A (cm^{-3})	1×10^{18}	1×10^{18}	1×10^{18}	1×10^{18}	1×10^{18}	1×10^{18}	1×10^{18}
N_D (cm^{-3})	0	0	0	0	0	0	
N_t (cm^{-3})	1×10^{14}	1×10^{14}	1×10^{14}	1×10^{14}	1×10^{14}	1×10^{14}	1×10^{14}

Table 3
Characteristics of interface used in heterojunction solar cells comprising Ag/FTO/ETL(In_2S_3,SnS_2,ZnSe)/$MoSe_2$/V_2O_5/Ni structures.

Interface	Defect type	Capture cross section: electrons/holes (cm^2)	Defect position above the highest EV (eV)	Reference for defect energy level	Energetic distribution	Total defect density (cm^{-2})
$MoSe_2$/ SnS_2	Neutral	1×10^{-19}	0.06	Above the highest E_v	Single	1.0×10^{10}
$MoSe_2$/ In_2S_3	Neutral	1×10^{-19}	0.06	Above the highest E_v	Single	1.0×10^{10}
$MoSe_2$/ ZnSe	Neutral	1×10^{-19}	0.06	Above the highest E_v	Single	1.0×10^{10}
V_2O_5/ $MoSe_2$	Neutral	1×10^{-19}	0.06	Above the highest E_v	Single	1.0×10^{10}

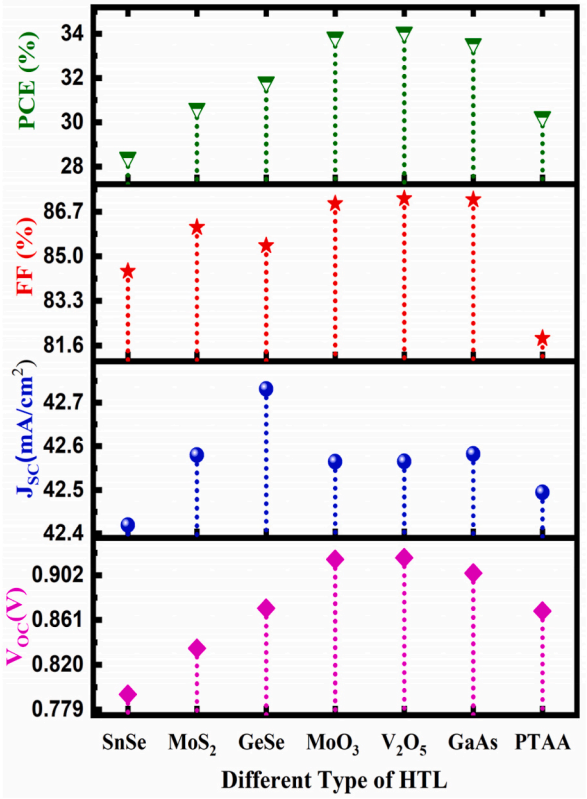

Fig. 2. Optimizing the HTL of $MoSe_2$ based solar cell depends on the performance of the cell, namely the PCE, V_{OC}, FF, and J_{SC} values.

Table 4
The values of the performance parameters for Ag/FTO/SnS_2/$MoSe_2$/HTL/Ni structures with different HTLs.

Structure	V_{OC} (V)	J_{SC} (mA/cm^2)	FF (%)	PCE (%)
FTO/SnS_2/$MoSe_2$/SnSe	0.79321	42.4197	84.4344	28.4103
FTO/SnS_2/$MoSe_2$/MoS_2	0.83519	42.580	86.1096	30.6226
FTO/SnS_2/$MoSe_2$/GeSe	0.87176	42.7317	85.4108	31.817
FTO/SnS_2/$MoSe_2$/MoO_3	0.91656	42.5650	87.0066	33.944
FTO/SnS_2/$MoSe_2$/GaAs	0.90395	42.5826	87.1627	33.5515
FTO/SnS_2/$MoSe_2$/PTAA	0.86921	42.4947	81.871	30.2405
FTO/SnS_2/$MoSe_2$/V_2O_5	0.91800	42.5654	87.1994	34.0734

performance indicators is therefore crucial. Fig. 3 shows how the defect (N_t) and doping density (N_A) of V_2O_5 affect the suggested SC's performance parameters. While other parameters stay the same, the values of N_t and N_A have been altered within the ranges of 10^{10} to 10^{17} cm^{-3} and 10^{12} to 10^{20} cm^{-3}, respectively. The PCE, V_{OC}, FF, and J_{SC} values do not significantly change as the HTL layer's N_t increases from 10^{10} to 10^{17} cm^{-3} and remain constant at 34.07 %, 0.9178 V, 87.1976 %, and 42.56542 mAcm^{-2}, as shown in Fig. 3 (a–d). At first, there is a steady trend in the parameter values of V_{OC} and PCE when the N_A of the HTL layer is increased up to 10^{17} cm^{-3}. After that, when the N_A exceeds 10^{17} cm^{-3}, it marginally rises.

Additionally, the initial values of J_{SC} and FF similarly exhibit a steady tendency as the N_A of the HTL layer is increased up to 10^{16} cm^{-3}. Following that, when the N_A exceeds 10^{16} cm^{-3}, it slightly rises. A higher concentration of N_A may lessen the recombination of

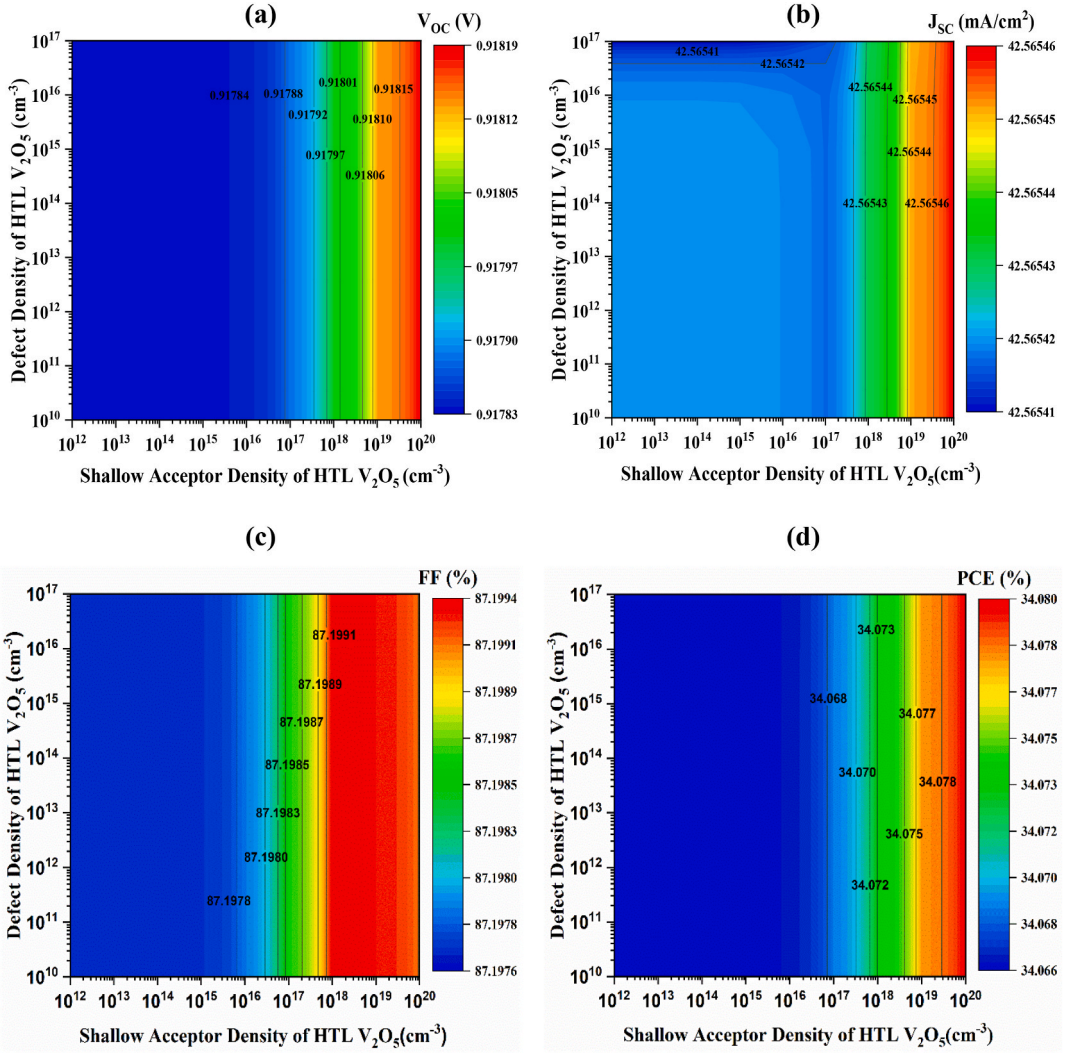

Fig. 3. Variations in photovoltaic performance characteristics (a) V_{OC} (b) J_{SC} (c) FF, and (d) PCE as a result of changes in HTL defect vs doping density.

carriers that aid in the appropriate transportation and carrier collection, leading to an increase in PCE, V_{OC}, FF, and J_{SC}. The increment in series resistance in the proposed SC is indicated by the reduction in FF in V_2O_5 HTL with decreasing N_A. To attain the maximum PCE of 34.07 %, the ideal N_t could be determined to be 10^{14} cm^{-3}, and the optimal N_A to be 10^{18} cm^{-3}, with a V_{OC} of 0.918 V, a J_{SC} of 42.565 $mAcm^{-2}$, and an FF of 87.19 %.

3.3. Band diagram of $MoSe_2$ setups using various ETLs

Three Electron Transport Layers (ETL) band configurations are shown in Fig. 4(a–c), which show band diagram changes that are exclusively related to the ETL, while the absorber layer and HTL stay unchanged. Since electron and hole extraction efficiency has a major impact on overall performance, optimizing band alignment is essential for improving device performance. When exposed to light, excitons produced in the absorber layer are transported to the ETL and HTL. The device keeps the single fermi level when there is no light. But as it gets lighter, the Fermi level splits into two quasi-Fermi levels, one for electrons and one for holes. The quasi-Fermi level for electrons is continuously higher in the HTL than the E_c and E_v levels, which coexist with two quasi-Fermi levels. When compared to F_n, E_c exhibits strikingly comparable behavior, as seen in Fig. 4. But F_p always lies higher than E_v for all ETLs combined. This kind of solar cell device's performance is highly affected by its conduction band offset (CBO) and valence band offset (VBO), which can both be positive or negative. Because of the decreased carrier recombination, a positive CBO (spike-like) is produced when the ETL material's Conduction Band Minimum (CBM) is greater than the absorber material.

This leads to superior PCE. Because photogenerated carriers are lost, PCE and J_{SC} are reduced when the positive CBO is greater than 4. On the other hand, when the CBM of the ETL is smaller than that of the active layer, a negative band alignment, sometimes referred to as a cliff-like alignment, happens. In general, a tiny spike (0–0.2 eV) is preferable for the ETL/Absorber interface. This keeps electrons from diffusing back into the absorber without impeding electron transport too much. There is a tiny spike (~0.2 eV) from SnS_2 CBM (4.1 eV) to $MoSe_2$ CBM (4.3 eV). The slight cliff shown by the VBM alignment helps with hole blocking. To guarantee that electrons may transfer from $MoSe_2$ to In_2S_3 and ZnSe with the least amount of resistance, the CBM of In_2S_3 and ZnSe should be somewhat greater than that of $MoSe_2$. However, in order to avoid electron blockage, a big surge should be avoided. A small cliff (0–0.2 eV) is typically preferred for absorber/HTL. This reduces recombination at the interface and promotes hole transport to the HTL. A cliff

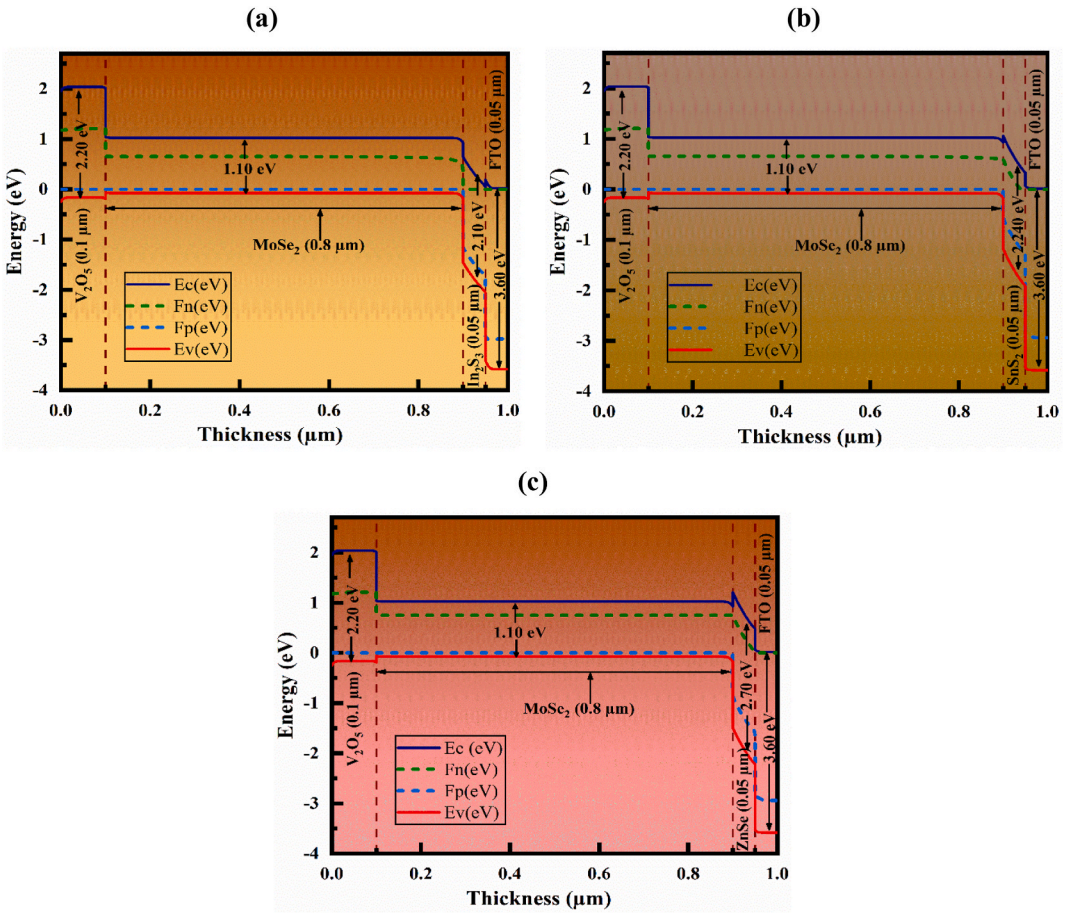

Fig. 4. Energy band diagram of Ag/FTO/ETL/$MoSe_2$/V_2O_5/Ni structures with (a) In_2S_3, (b) SnS_2, and (c) ZnSe ETLs.

(~0.7 eV) arises between $MoSe_2$ VBM (5.1 eV) and V_2O_5 VBM (4.4 eV), which enhances hole transport but requires careful optimization. Similar to this, when the valence band maximum (VBM) of the HTL is higher than that of the absorber material, J_{SC} may increase and a positive VBO, also known as spike-like alignment, is seen. Conversely, when the HTL's VBM is less than the absorber material's, a negative VBO, also known as a cliff-like alignment, results, which can lower the V_{OC}. The different cliff and spike alignments shown in Fig. 4 have an immediate impact on this solar cell's performance.

3.4. Influence of thickness of the absorber and ETL layer

As an absorber layer, $MoSe_2$ significantly influences solar cell performance. The thickness of the absorber is a crucial parameter that remarkably impacts the device [52,53]. In our simulations, we focus on performance metrics such as FF, J_{SC}, V_{OC}, and PCE as functions of absorber thickness, changing from 0.3 μm to 3.0 μm, as shown in Fig. 5(a). To maximize photon absorption and electron-hole pair generation, the absorber layer should have an optimal thickness. Therefore, the performance of solar cells primarily depends on the absorber layer's thickness. The illumination spectrum utilized is AM 1.5, while the operational temperature is fixed at 300 K. We maintain the doping concentration at $N_A = 10^{18}$ cm^{-3} for the absorber layer and 0.1 μm thickness for HTL, with $N_A = 10^{18}$ cm^{-3}. For both SnS_2 and ZnSe ETLs, increasing absorber thickness during the optimization process increased the reverse saturation current, but even a small increase in thickness resulted in a drop in V_{OC}. However, despite variations in thickness, the V_{OC} for the In_2S_3 ETL stayed largely consistent. For all three ETLs, the J_{SC} improved up to 1.5 μm in thickness, which was attributable to increased generation of charge carriers within the absorber layer. These changes in J_{SC} and V_{OC} demonstrate a pattern consistent with research findings from publications [31,54]. The FF remained almost unchanged and PCE increases gradually with the increase of absorber thickness for SnS_2 and In_3S_3 ETLs, but decrease for ZnSe ETL. The penetration depth of light into the absorber layer guides the choice of layer thicknesses in solar cells to ensure efficient light absorption. The absorber must be thick enough to capture photons but not so thick that it increases recombination losses. Balancing light absorption and charge collection is crucial, considering the solar spectrum's range. Adjacent layers should be thin to let light pass while providing necessary functions. Simulations help optimize thicknesses for maximum efficiency. We have chosen 800 nm as the thickness of absorber layer for balancing the whole structure. With that thickness, we have got the maximum performances. A larger recombination rate resulted from the absorption of more photons as the absorber layer's thickness grew. But a small absorber layer could only hold so much light, which meant that the electrodes had to extract a large amount of carrier and the PCE was reduced. In order to achieve maximum efficiency, light absorption and carrier mobility must be balanced, since an excessively thick absorber layer reduces PCE. As a result, 800 nm was found to be the ideal thickness for the $MoSe_2$ absorber in this investigation for improved performance with SnS_2, In_2S_3, and ZnSe ETLs. For the In_2S_3 ETL, the optimal PCE was found to be 29.3574 %, with an FF of 79.3968 %, a J_{SC} of 42.5516 $mAcm^{-2}$, and a V_{OC} of 0.868957 V. The SnS_2 ETL achieved a PCE of 34.0734 %, an FF of 87.1994 %, a J_{SC} of 42.5654 $mAcm^{-2}$, and a V_{OC} of 0.918005 V. Meanwhile, the ZnSe ETL resulted in a PCE of 30.6699 %, an FF of 78.6293 %, a J_{SC} of 42.4789 $mAcm^{-2}$, and a V_{OC} of 0.918235 V.

The impact of the thickness of the SnS_2, In_2S_3, and ZnSe ETLs on solar cell performance is examined in Fig. 5(b). The thicknesses of the ETL layer were varied simultaneously within the ranges of 0.02 μm–0.49 μm, respectively, using previously optimized parameters. Also, the thickness of the ETL layer has a significant effect on the other electrical characteristics of the PV cell. Even though the

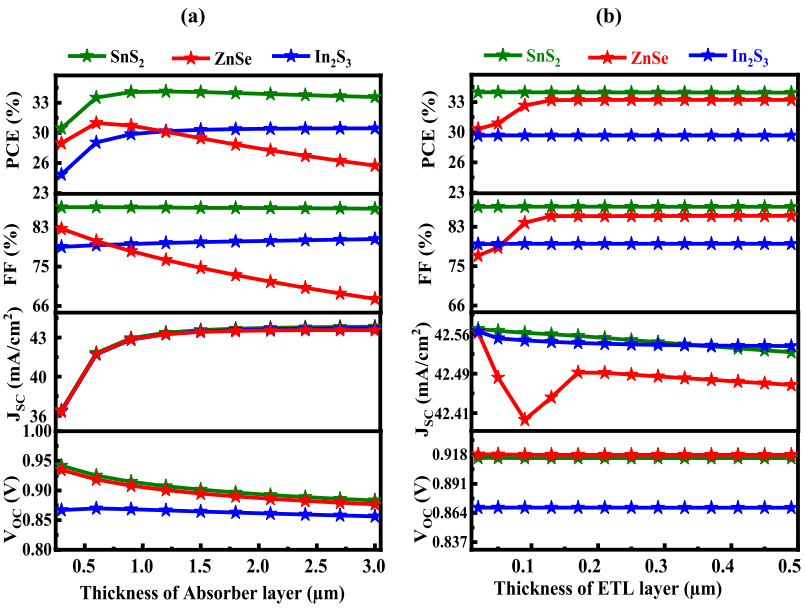

Fig. 5. The influence of thickness in (a) absorber, and (b) ETL layers on solar cell performance with SnS_2, In_2S_3, and ZnSe ETLs.

thickness of the ETL layer increased, devices using SnS_2, In_2S_3, and ZnSe ETLs showed almost consistent V_{OC} of 0.9158 V, 0.8689 V, and 0.9178 V, respectively. SnS_2 saw a small decrease in J_{SC} from 42.5704 to 42.4982 mA/cm^2, In_2S_3 from 42.5702 to 42.5370 mA/cm^2, and ZnSe from 42.5699 to 42.4314 mA/cm^2. For SnS_2 and In_2S_3 ETLs, the FF and PCE stayed relatively constant at 87.20 % and 79.40 %, and 34.05 % and 29.34 %, respectively, with increasing thickness. On the other hand, when the ETL thickness increased using ZnSe ETL, the FF and PCE increased from 79.33 to 85.33 % and from 31.011 to 33.242 %, respectively.

3.5. Influence of doping density of the absorber and ETL

To assess the impact of the $MoSe_2$ absorber acceptor concentration (N_A) on solar cell performance (J_{SC}, V_{OC}, FF, and PCE) with all three ETLs, we varied the N_A from 10^{13} to 10^{20} cm^{-3}, as illustrated in Fig. 6(a). The absorber's N_A grew during optimized performance, while the SC's V_{OC} and PCE didn't alter until N_A of 10^{16} cm^{-3}, at which point they started to rise. According to a previous publication [31,55], the hole's Fermi energy level decreases as the absorber layer's N_A increases, increasing the V_{OC}. Along with the N_A of the absorber layer, the built-in potential increases. The J_{SC} for SnS_2 and In_2S_3 ETLs did not significantly alter when absorber N_A increased. However, for ZnSe ETL, the J_{SC} dropped when the N_A went over 10^{18} cm^{-3}. However, the FF rose as the absorber layer's N_A value exceeded 10^{15} cm^{-3}. For SnS_2 ETL, the maximum values obtained by the V_{OC}, J_{SC}, FF, and PCE were 1.035 V, 42.562 mAcm^{-2}, 88.49 %, and 38.99 %; for In_2S_3 ETL, the maximum values were 0.897 V, 42.557 mAcm^{-2}, 85.19 %, and 32.54 %; and for ZnSe ETL, the maximum values were 1.033 V, 42.561 mAcm^{-2}, 81.95 %, and 32.63 % with the variation of absorber N_A from 10^{13} to 10^{20} cm^{-3}. This could be the outcome of the report's observation that there are more defect states when the absorber layer's N_A rises.

The PV characteristics for all three ETLs are shown in Fig. 6(b) as a function of the donar concentration (N_D). For SnS_2 ETL, FF, J_{SC}, V_{OC}, and PCE remained constant at 87.19 %, 42.56 mAcm^{-2}, 0.918 V, and 34.07 % with increasing N_D from 10^{13} cm^{-3} to 10^{20} cm^{-3}. After that, there was a noticeable increase in FF, J_{SC}, and PCE, remaining constant up to 10^{15} cm^{-3} for ZnSe ETL (64.61–86.98 %, 42.24 to 42.54 mAcm^{-2}, and 25.08–33.96 %), but V_{OC} remaining steady at 0.918 V. After that, there was a noticeable increase in the FF, V_{OC}, and PCE, which remained constant for In_2S_3 ETL up to 10^{18} cm^{-3} (79.47–85.56 %, 0.868–0.884 V, and 29.38–32.20 %), whereas J_{SC} was constant at 42.55 mAcm^{-2}. At an N_D of 10^{17} cm^{-3}, SnS_2 ETL was found to be the optimal structure. The substantial drop in series resistance (R_s) and the rise in the internal electric field are probably to blame for this improvement in FF. This study's conclusions are consistent with those of earlier research [56,57].

3.6. Changes on PV parameters with the variation of thickness and defect density in absorber layer for various ETL

The effect of defect density (N_t) and absorber thickness on PV characteristics with SnS_2 ETL is shown in Fig. 7. The effects of N_t between 10^{10} and 10^{17} cm^{-3} and thickness ranges between 0.4 and 2.8 μm are investigated in order to assess the device's performance. Fig. 7(a) demonstrates that the V_{OC} of the SC with SnS_2 ETL remains consistent regardless of the thickness of the $MoSe_2$ layer. Fig. 7(a) illustrates how the N_t swings between 10^{10} and 10^{17} cm^{-3}, which negatively impacts the V_{OC} and reduces it from 1.1589 to 0.6841 V. Conversely, J_{SC} has a maximum value of 43.80 mAcm^{-2} when thicknesses reach 1.6 μm and N_t falls below 10^{15} cm^{-3}, respectively (Fig. 7(b)). There is a 4.548 mAcm^{-2} decrease in J_{SC} when the thickness is reduced from 2.8 to 0.4 μm with N_t less than 10^{14} cm^{-3}. Since increasing N_t causes the diffusion length of the charge carriers to decrease and the number of recombination carriers in the absorber layer to rise, we may conclude that N_t directly affects efficiency. Fig. 7(c) demonstrates that the FF reaches its highest value of

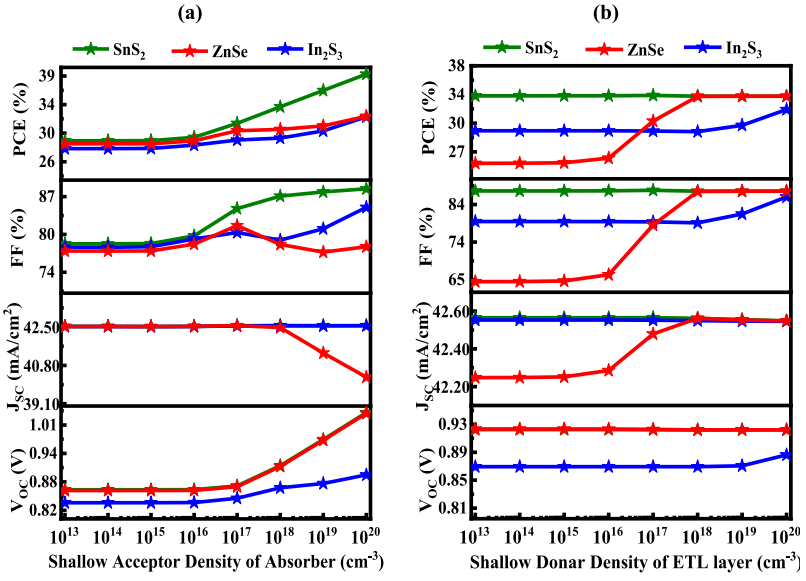

Fig. 6. The influence of doping concentration in (a) absorber, and (b) ETL layers on solar cell performance.

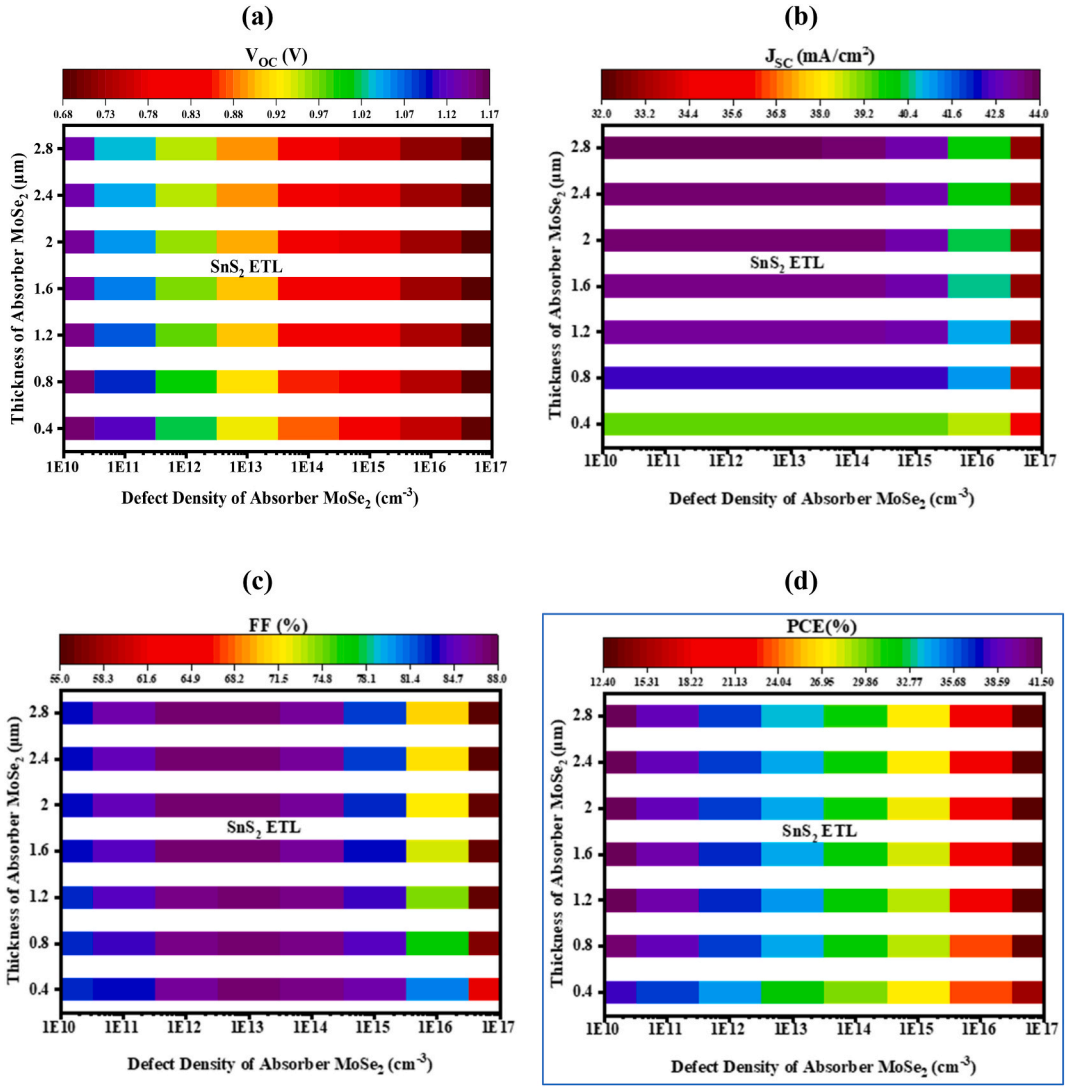

Fig. 7. Impact of the thickness of $MoSe_2$ absorber vs bulk defect density modifications on PV parameters; (a) V_{OC} (b) J_{SC} (c) FF and (d) PCE using SnS_2 ETL.

87.24 % when the N_t is equal to 10^{13} cm^{-3}. However, there is a significant drop in FF to 55.53 % when the N_t is raised above 10^{16} cm^{-3}. Because of the acceleration of the recombination process that destroys the charge carriers, performance falls as N_t grows. Reduced N_t leads to improved PV performance because of the long carrier diffusion length and minimal recombination process. The absorbers must have a low N_t and a high carrier concentration for better PCE. Thus, with a layer thickness of 0.8 µm and a N_t of 10^{13} cm^{-3}, the greatest and best PCE of 34.07 % was attained, accounting for trade-offs among PV characteristics. This SC achieved a V_{OC} of 0.918 V, a J_{SC} of 42.565 $mAcm^{-2}$, and an FF of 87.19 % at these given conditions.

The absorber's N_t has a major effect on SC efficiency with In_2S_3 ETL. Photovoltaic energy is produced when light interacts with the absorber layer. Fig. 8(a–d) illustrate the impact of absorber N_t between 10^{10} and 10^{17} cm^{-3}, whose thickness varies between 0.4 and 2.8 µm with In_2S_3 ETL. Changes in absorber layer thickness from 0.4 to 2.8 µm and N_t from 10^{10} and 10^{17} cm^{-3} resulted in a variation in PCE, FF, J_{SC}, and V_{OC} with In_2S_3 ETL from 30.30 to 19.32 %, 84.22 to 78.61 %, 43.792 to 34.370 $mAcm^{-2}$, and 0.879 to 0.682V, respectively. Fig. 8(a–d) show that when the absorber layer thickness is greater than 0.8 µm and the N_t is less than 10^{14} cm^{-3}, the V_{OC}, J_{SC}, FF, and PCE reach their highest levels. Thus, taking into consideration trade-offs among PV properties, the maximum and optimum PCE of 29.3574 % was achieved with a layer thickness of 0.8 µm and a N_t of 10^{13} cm^{-3}. Under these circumstances, this SC produced a V_{OC} of 0.868957 V, a J_{SC} of 42.5516 $mAcm^{-2}$, and an FF of 79.3968 %.

The N_t of the absorber has a significant impact on SC efficiency with ZnSe ETL. Photovoltaic energy is produced when light interacts with the absorber layer. The effect of absorber N_t with thickness ranges between 10^{10} and 10^{17} cm^{-3} and 0.4 and 2.8 µm is shown in Fig. 9(a–d). Decreases in the device's PCE, FF, J_{SC}, and V_{OC} with ZnSe ETL were caused by changes in the absorber layer thickness from 0.4 to 2.8 µm and N_t from 10^{10} and 10^{17} cm^{-3} and these changes occurred from 41.02 to 0.432 %, 82.38 to 13.42 %, 43.810 to 2.799

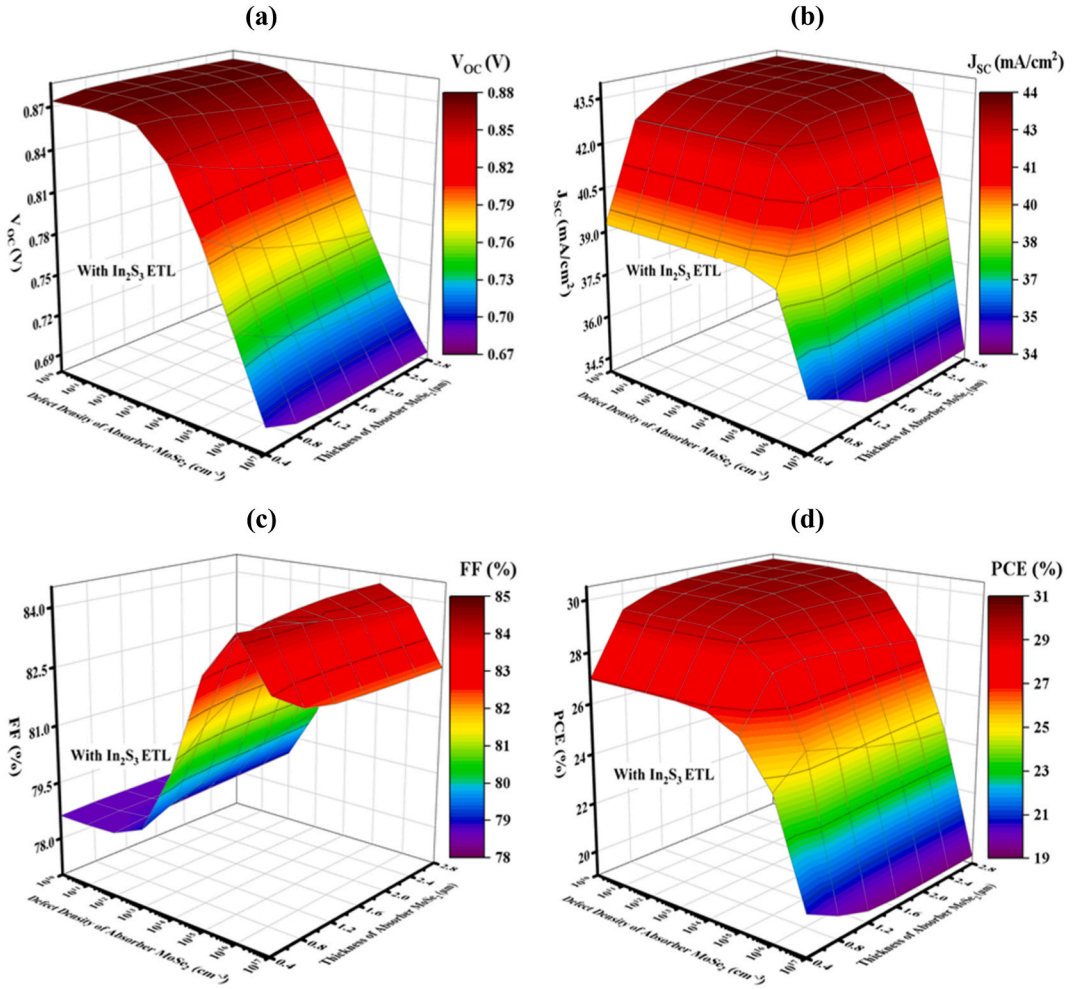

Fig. 8. Impact of the thickness of $MoSe_2$ absorber vs bulk defect density modifications on PV parameters; (a) V_{OC} (b) J_{SC} (c) FF and (d) PCE using In_2S_3 ETL.

mAcm^{-2}, and 1.158 to 0.734V, respectively. Fig. 9(a–d) demonstrate that the V_{OC}, J_{SC}, FF, and PCE reach their maximum levels when the absorber layer thickness is greater than 1.2 μm and the N_t is less than 10^{12} cm^{-3}. Thus, with an absorber layer thickness of 0.8 μm and a N_t of 10^{13} cm^{-3}, the greatest and optimal conversion efficiency of 30.6699 % was obtained while accounting for trade-offs among PV attributes. In these conditions, the solar cell generated an FF of 78.6293 %, a J_{SC} of 42.4789 mAcm^{-2}, and a V_{OC} of 0.918235 V.

3.7. Impact of the interface defect density

We studied the interface defect density (N_{tf}) across different interfaces to improve the photoelectric characteristics of SCs. However, it is imperative to evaluate the impact of N_{tf} on SC performance, as these defects play a crucial role in influencing SC outputs by promoting carrier recombination, thereby diminishing the PCE of the SC. Understanding the correlation between N_{tf} and performance has prompted researchers to devise strategies for minimizing defect formation and enhancing the PCE of SC. Additionally, investigating the effects of N_{tf} on SCs contributes to a deeper comprehension of SC physics, paving the way for the development of novel materials and fabrication techniques. The PV properties of newly designed $MoSe_2$-absorber-based SCs are influenced by N_{tf} at V_2O_5/$MoSe_2$, $MoSe_2$/In_2S_3, $MoSe_2$/SnS_2, and $MoSe_2$/ZnSe, as illustrated in Fig. 10.

The N_{tf} was varied from 10^9 cm^{-2} to 10^{17} cm^{-2}, and the corresponding PV outputs were analyzed. For the V_2O_5/$MoSe_2$ interface, increasing N_{tf}, significantly reduced PCE, FF, and V_{OC} from 34.074 to 18.077 %, 87.199 to 67.717 %, and 0.9180 to 0.7104 V. N_{tf} can create recombination centres, which diminish carrier transport efficiency in the device, leading to reductions in V_{OC} and FF. At the $MoSe_2$/In_2S_3 interface, higher N_{tf} had the greatest impact on PCE, which decreased from 32.988 to 8.042 %. V_{OC} and FF also dropped from 0.9121 to 0.2820 V, and 84.991 to 67.617 %. J_{SC} remained almost stable for both V_2O_5/$MoSe_2$, and $MoSe_2$/SnS_2 interfaces with the increasing of N_{tf} at 42.56 mA/cm^2, and 42.55 mA/cm^2. For the $MoSe_2$/SnS_2, and $MoSe_2$/ZnSe interface, increasing N_{tf}, significantly reduced PCE, FF, J_{SC}, and V_{OC} from 34.075 to 4.499 %, and 30.677 to 0.357 %, 87.201 to 63.125 %, and 78.638 to 54.220 %,

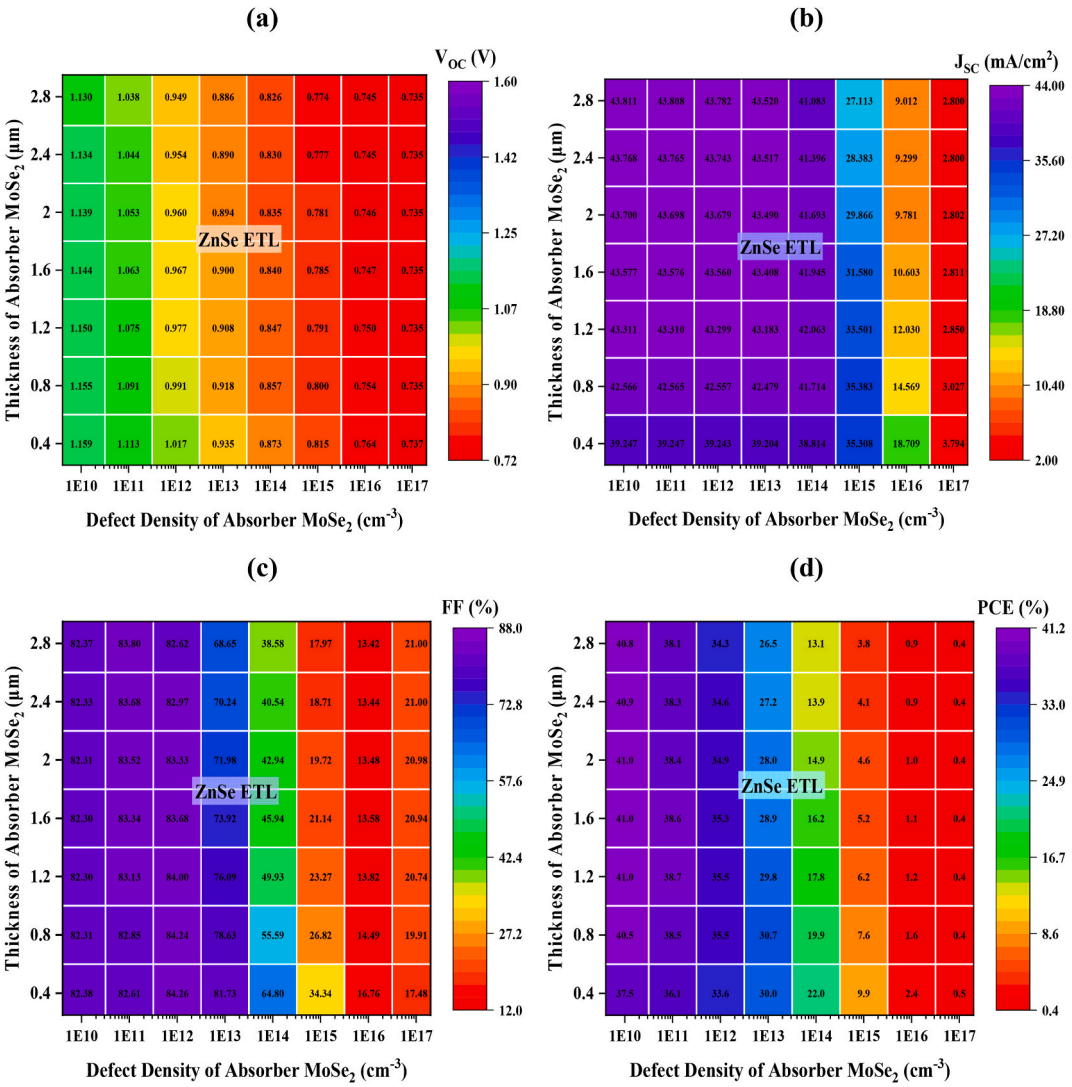

Fig. 9. Impact of the thickness of $MoSe_2$ absorber vs bulk defect density modifications on PV parameters; (a) V_{OC} (b) J_{SC} (c) FF and (d) PCE using ZnSe ETL.

42.565 to 1.081 mA/cm^2, and 42.482 to 0.620 mA/cm^2, 0.9180 to 0.6432 V, and 0.9182 to 0.7314 V. When there are interface challenges, series resistance might increase significantly [58]. The decline in performance is caused by the greater rate of interface carrier recombination that occurs when N_{tf} rises [59,60]. Thus, it is suggested that N_{tf} at the V_2O_5/$MoSe_2$, $MoSe_2$/In_2S_3, $MoSe_2$/SnS_2, and $MoSe_2$/ZnSe layers have a major role in determining the performance characteristics of PV devices [61,62].

3.8. Impact of the rate of generation-recombination and carrier concentration

The carrier production and recombination rates for the Ag/FTO/ETL(In_2S_3,SnS_2,ZnSe)/$MoSe_2$/V_2O_5/Ni structures across many sites are shown in Fig. 11(a) and (b). During carrier creation, an electron moves from the valence band (VB) to the conduction band (CB), forming pairs of electrons and holes, with the hole staying in the VB. $MoSe_2$ generates more carriers as a result of this transition, which releases electrons and holes. Notably, for Ag/FTO/ETL(In_2S_3,SnS_2,ZnSe)/$MoSe_2$/V_2O_5/Ni structured SCs, the generation rate is lowest around 0.01 μm and highest at approximately 0.9 μm when In_2S_3/SnS_2/ZnSe ETL is present. The differing photon absorption rates at various sites are the cause of this discrepancy. G(x) can be found more easily with the help of equation (7), and the N_{phot} (λ, x) of the SCAPS-1D model uses the incoming photon flux to measure the creation of pairs of electrons and holes.

$$G(\lambda, x) = \alpha\ (\lambda, x).N_{phot}(\lambda, x) \tag{7}$$

Electrons and holes are recombinant in the conduction band of solar systems. The density and longevity of these charge carriers play a major role in determining the recombination rates in carefully engineered and optimized SCs. SC recombination is also

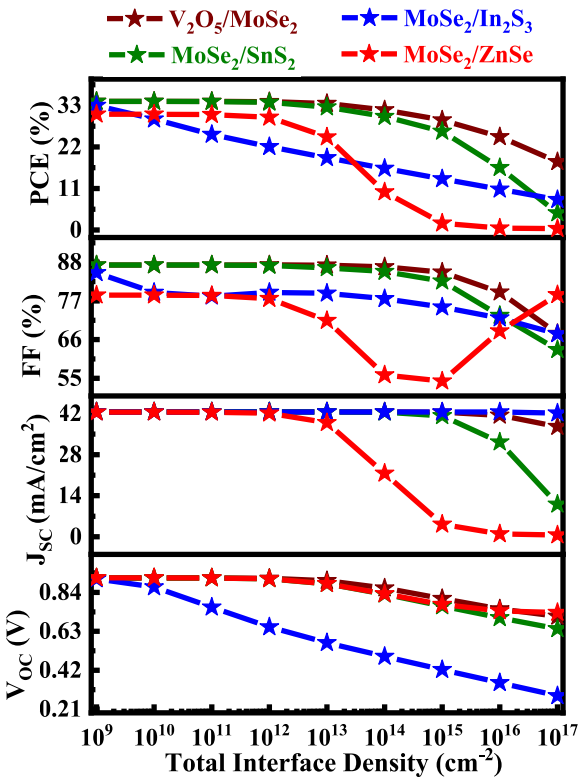

Fig. 10. Defect effects on PV characteristics at the $V_2O_5/MoSe_2$, $MoSe_2/In_2S_3$, $MoSe_2/SnS_2$, and $MoSe_2/ZnSe$ interfaces.

significantly influenced by the defect states in each layer. The number of electrons from the conduction band that pair with holes in the valence band is greater when they pass the energy barrier.

Furthermore, the kinetics of electron-hole recombination are influenced by the energy levels linked to this transition. The differences in the $MoSe_2$ absorber layer thickness, In_2S_3/SnS_2/ZnSe ETLs, and their consequences on the concentrations of electron and hole carriers are depicted in Fig. 11(c) and (d). The hole concentration in the $MoSe_2$ absorber is affected by these variations in absorber thickness because they result in different densities of states (DOS) within the valence bands. In particular, when comparing electron and hole densities, the existence of larger carrier concentrations is more significant [63,64]. According to this study, using SnS_2 as the ETL in conjunction with $MoSe_2$ decreases electron-hole recombination and increases carrier production, increasing the absorber material's efficiency. These advancements may open the door to the creation of highly effective SCs.

3.9. Absorption coefficient of all layers

The power conversion efficiency (PCE) of a solar cell is greatly influenced by the optical absorption coefficient, a crucial parameter for assessing a material's capacity to absorb light energy. The SCAPS-1D simulator computes the absorption coefficient for each layer. When it comes to solar cells, the initial absorption peak is especially important since it indicates the precise light wavelengths that a material can absorb [65–67]. FTO/SnS_2/$MoSe_2$/V_2O_5 SC structure is associated with $MoSe_2$, V_2O_5, SnS_2, and FTO materials. The absorption coefficient changes at various wavelengths for $MoSe_2$, V_2O_5, SnS_2, and FTO materials are shown in Fig. 12. Remarkably, for $MoSe_2$, V_2O_5, and SnS_2 materials, the absorption coefficient shows strong peaks at 200 nm wavelength, while for FTO, this peak is at 172 nm wavelength. The greatest absorption points of each substance in the visible and UV light spectrums are shown by their optical absorption spectra. The absorption peaks with the highest values are 215319.74 cm^{-1} (Fig. 12(a)), 134838.03 cm^{-1} (Fig. 12(b)), 132958.85 cm^{-1} (Fig. 12(c)), and 100000 cm^{-1} (Fig. 12(d)) for $MoSe_2$, V_2O_5, SnS_2, and FTO materials, respectively.

3.10. Operating temperature's effect on a solar cell's performance

Fig. 13 provides insights into the impact of temperature on the performance of optimum Ag/FTO/SnS_2/$MoSe_2$/V_2O_5/Ni structured SC, spanning a temperature range of 275–475 K. The results reveal that as temperature increases, there's a tendency for J_{SC} to increase slightly while the FF, V_{OC}, and PCE decrease. This observation suggests that elevated temperatures enhance the thermal mobility of carriers within the solar cell, potentially leading to higher J_{SC}. However, increased temperatures may also cause the absorber layer to behave as an ohmic conductor, impeding carrier flow and resulting in the conversion of electrical energy into heat, thereby reducing

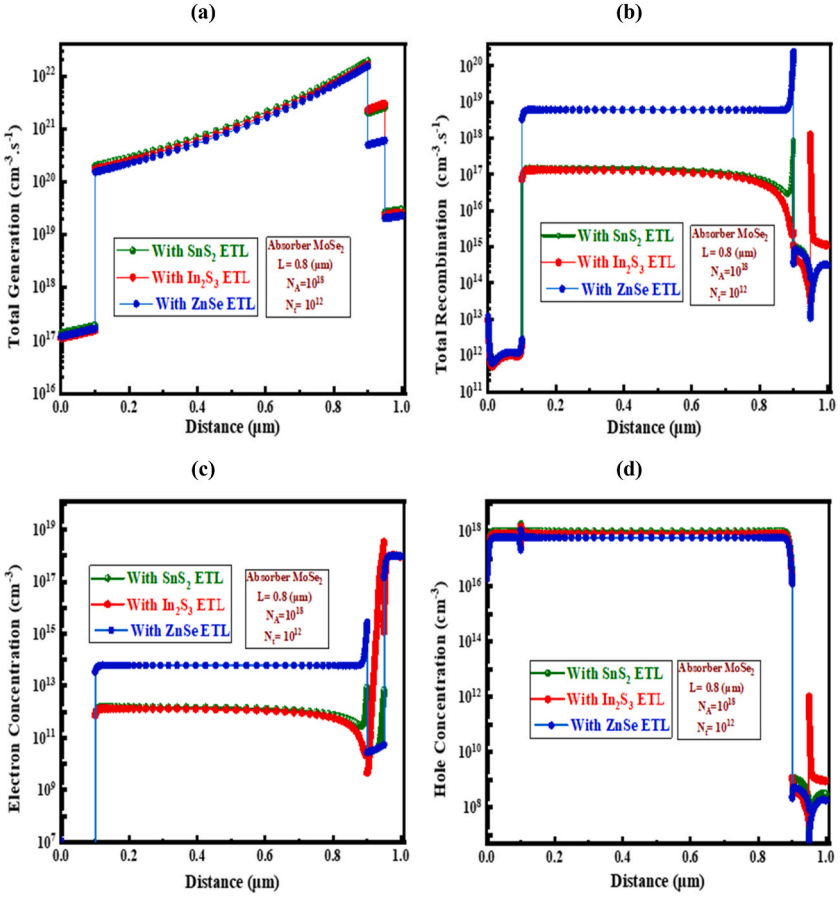

Fig. 11. Impacts of the thickness of the absorber layer on (a) total generation, (b) recombination, (c) electron concentration, and (d) hole concentration.

FF, V_{OC}, and PCE [68,69]. The limited thermal dissipation within different components of the SC can exacerbate temperature rise, posing a risk of device damage. Therefore, it is crucial to carefully consider the operational limits of each absorber layer during the fabrication of such heterojunction SCs. The temperature dependence is evident in the slight increase of J_{SC} from 42.5644 mA/cm^2 at 275 K to 42.5695 mA/cm^2 at 475 K. Conversely, V_{OC}, and FF decreases from 0.940 V to 0.745 V, and 88.19 %–79.78 % with increasing temperature. The PCE reaches its highest value of 35.30 % at lower temperatures, declining to 25.12 % as temperature rises. Moreover, there's a noticeable steeper temperature gradient with an average efficiency decrease of 0.0509 %/K for the optimized Ag/FTO/SnS_2/$MoSe_2$/V_2O_5/Ni structure.

3.11. The impact of the series and shunt resistances on the PV performance

The impact of shunt resistance (R_{sh}) and series resistance (R_s) on the optimum Ag/FTO/SnS_2/$MoSe_2$/V_2O_5/Ni SC device is examined in Fig. 14. The combined effects of bulk resistance, front and rear metallic contact resistance, and terminal resistance in the circuit result in the R_s of a solar cell [70]. Lower R_s and larger R_{sh} are essential for increasing the SC's efficiency [71]. Furthermore, the V_{OC} and J_{SC} are impacted by the values of these resistances. Using SCAPS-1D, the values of R_s and R_{sh} are varied to observe the impact on the efficiency of the recommended and traditional SCs, where R_s is measured from 1 to 10 Ω-cm^2 and R_{sh} is measured from 10 to 10^{10} Ω-cm^2. V_{OC} is strongly dependent on R_{Sh}, as Fig. 14(a) demonstrates that raising the R_s by itself does not cause a significant rise in the V_{OC}. A high J_{SC} at 1 Ω-cm^2 R_s and 10^{10} Ω-cm^2 R_{sh} is shown in Fig. 14(b). The FF is mostly decreased by this R_s, keeping it from rising to 100 % as shown in Fig. 14(c). The maximum PCE of 32.37 % can be achieved with a R_s of 1 Ω-cm^2 and a R_{sh} of 10^6 Ω-cm^2, as shown in Fig. 14(d). We may infer from Fig. 14 that when the R_s and R_{sh} shift from 1 to 10 Ω-cm^2 and 10 to 10^{10} Ω-cm^2, respectively, the PCE, FF, J_{SC}, and V_{OC} vary from 32.37 % to 2.25 %, 82.81 to 25 %, 42.5653 to 21.2823 mA cm^{-2}, and 0.9188 to 0.4256 V. The research indicates that in order to achieve higher performance, the R_s must be kept as low as feasible and the R_{sh} as high as possible.

3.12. J-V and Q-E characteristics

$MoSe_2$ is a promising material for use as an absorber layer in photovoltaic cells. The solar cell's quantum efficiency (Q-E) and

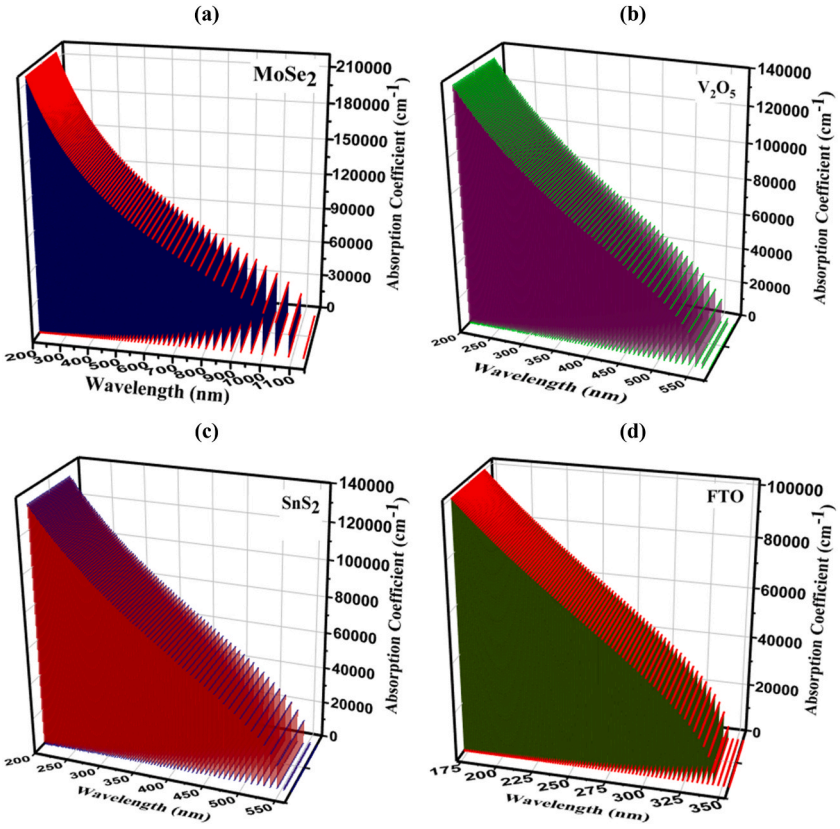

Fig. 12. Absorption coefficient of Ag/FTO/SnS_2/$MoSe_2$/V_2O_5/Ni optimal solar cell structure for (a) $MoSe_2$, (b) V_2O_5, (c) SnS_2, and (d) FTO materials.

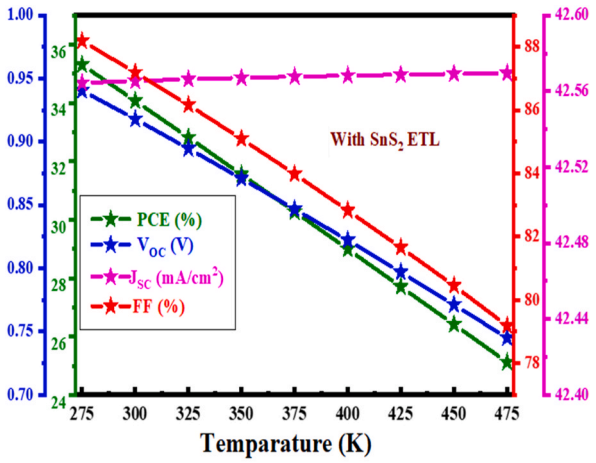

Fig. 13. Effects of temperature changes on the PV characteristics of the optimum Ag/FTO/SnS_2/$MoSe_2$/V_2O_5/Ni structure.

current-voltage (J-V) properties are greatly influenced by the thickness of the $MoSe_2$ layer [72,73]. Generally speaking, a thicker layer of $MoSe_2$ absorber increases light absorption and produces more photocurrent, which raises the J_{SC}. A thicker layer, however, would also result in increased recombination losses, which would lower the FF and V_{OC}, thus lowering the solar cell's overall efficiency [74]. The latest researches have shown that manufacturing methods, doping levels, and device design all affect the ideal thickness of $MoSe_2$ absorber layers in high-efficiency SCs [44,69]. Sometimes efficiency can be increased by using thinner $MoSe_2$ absorber layers since they improve charge carrier collection and decrease recombination losses. The thickness of the absorber layer has an important effect on photocurrent generation and photon absorption, which in turn affects Q-E. Since thicker $MoSe_2$ layers absorb more photons, they

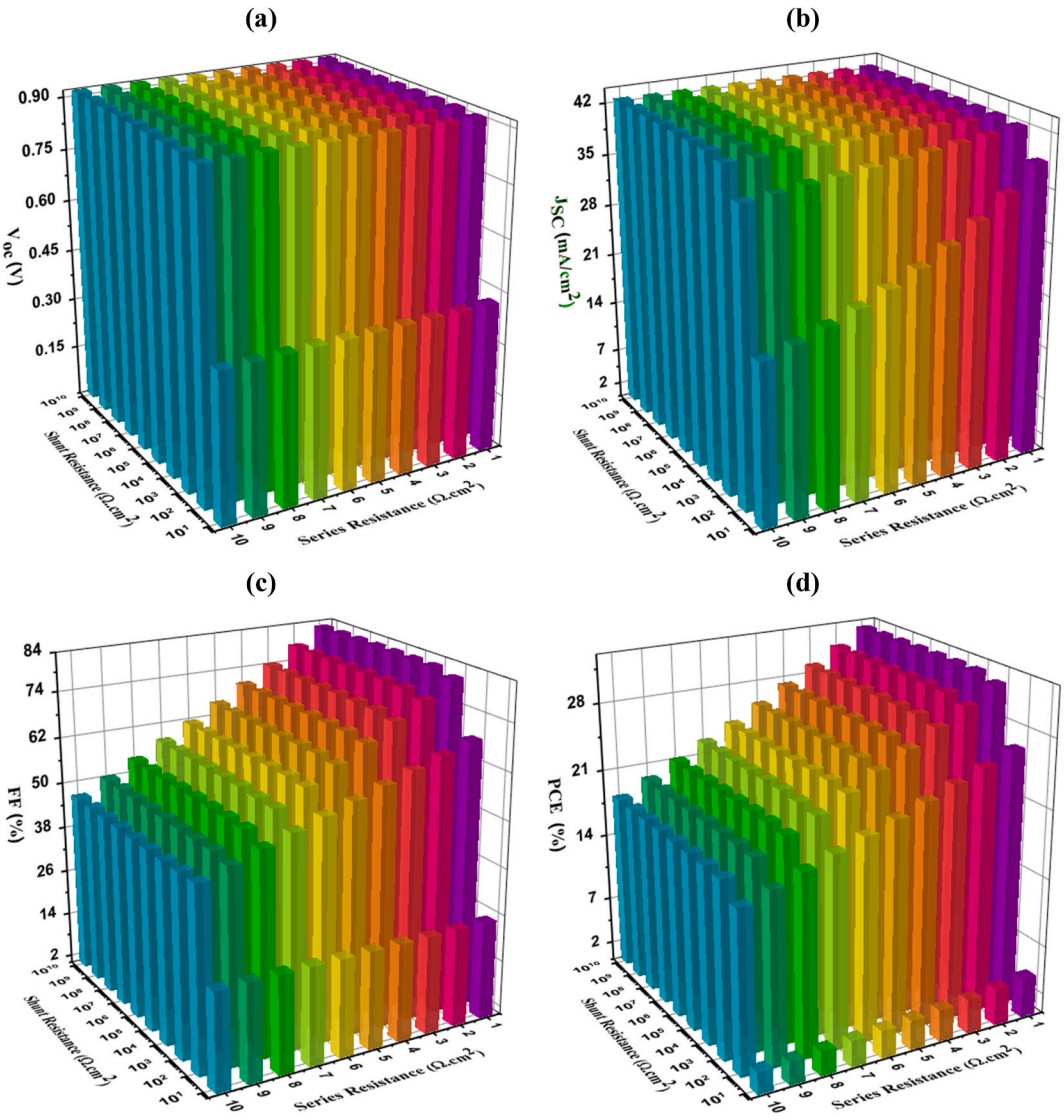

Fig. 14. Impact of the series vs shunt resistance modifications on PV parameters; (a) V_{OC} (b) J_{SC} (c) FF and (d) PCE for the optimum Ag/FTO/SnS_2/$MoSe_2$/V_2O_5/Ni structure.

can attain greater Q-E at longer wavelengths. On the other hand, overly thick layers can absorb light too deeply, which would reduce the efficiency of charge carrier collection and, in turn, Q-E.

For the Ag/FTO/SnS_2/$MoSe_2$/V_2O_5/Ni structure, the J-V and Q-E characteristics with changes in the thickness of the absorber layer are shown in Fig. 15. The optimized setup's PCE with V_2O_5 HTL and SnS_2 ETL attained a maximum of 34.07 %, with a V_{OC} of 0.918 V, a J_{SC} of 42.565 $mAcm^{-2}$, and an FF of 87.19 %. Interestingly, the optimized structure's current density zeroes out at 0.91 V. It is important to keep in mind that previous studies, as Fig. 15(a) illustrates, have consistently shown that current density decreases as voltage increases [75,76]. The QE profiles span a wavelength range of 300–1200 nm, as shown in Fig. 15(b). The QE for the Ag/FTO/SnS_2/$MoSe_2$/V_2O_5/Ni structure starts at about 100 % and progressively drops to 0 % as the wavelength gets closer to 1130 nm. The J-V characteristics results are consistent with this decline in QE.

3.13. Optimized device in compared to earlier researches

Researchers that have been studying $MoSe_2$-based solar cells in recent years have first observed poor performance when using ZnS as the electron transport layer (ETL). In spite of this, ongoing research has produced an important discovery: earlier this year saw a peak efficiency of 29.94 %. This trend shows that the performance of $MoSe_2$-based photovoltaics has been steadily improving year over year. This work regarding Ag/FTO/ETL/$MoSe_2$/V_2O_5/Ni optimum structure (as shown in Fig. 16) remarkably reports an astounding 34.0734 % maximum efficiency for $MoSe_2$-based solar cells, which is made possible by using V_2O_5 as the HTL and SnS_2 as the ETL, with

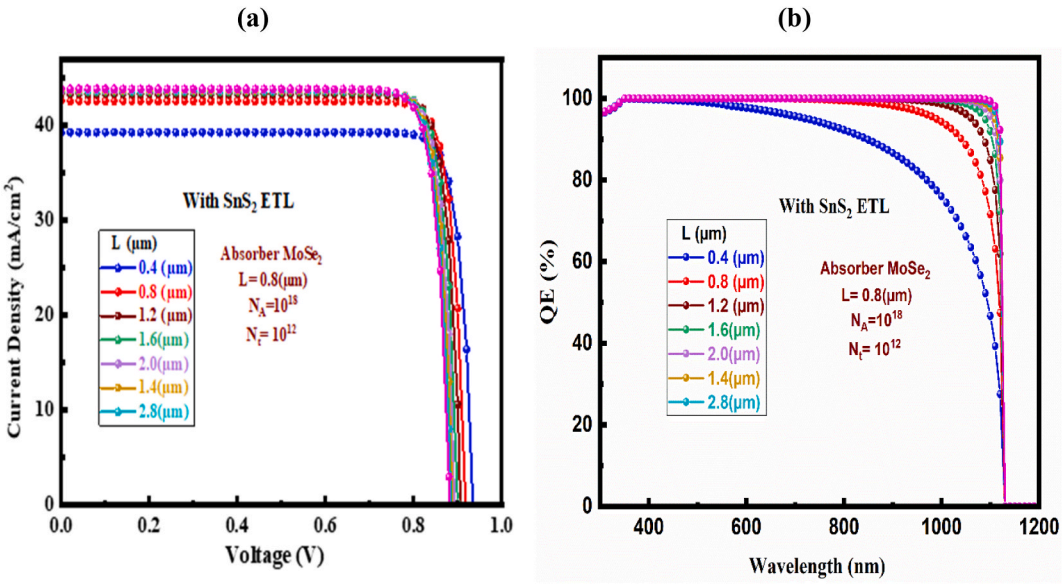

Fig. 15. (a) J–V and (b) QE curves of the optimum Ag/FTO/SnS_2/$MoSe_2$/V_2O_5/Ni structure.

a V_{OC} of 0.918 V, a J_{SC} of 42.565 mAcm^{-2}, and an FF of 87.19 %. Table 5 presents a comparison between the output performance values of this study and those from previous research.

Several factors can affect the performance of Ag/FTO/ETL/$MoSe_2$/V_2O_5/Ni solar cells during experimental fabrication, leading to discrepancies between experimental and simulated efficiencies:

a. **Material Quality**: Imperfections and defects in the materials can significantly reduce efficiency.
b. **Interface Quality**: Poor interfaces between layers can lead to high recombination rates and reduced charge transport.
c. **Thickness Control**: Inconsistent or incorrect layer thicknesses can impact light absorption and carrier collection.
d. **Contamination**: Presence of impurities can introduce trap states that hinder carrier mobility.
e. **Fabrication Conditions**: Variations in temperature, pressure, and deposition methods can affect layer uniformity and adhesion.
f. **Device Architecture**: Deviations from the ideal structure used in simulations can alter electrical and optical properties.
g. **Carrier Mobility**: Lower than expected carrier mobility can reduce the efficiency of charge transport.
h. **Recombination Losses**: Higher recombination rates in the experimental device can decrease open-circuit voltage and fill factor.
i. **Contact Resistance**: High resistance at the contacts can lead to significant power losses.
j. **Measurement Inaccuracies**: Errors in measuring efficiency and other parameters can lead to apparent discrepancies.

These factors highlight the complexities and challenges in translating simulation results to real-world devices.

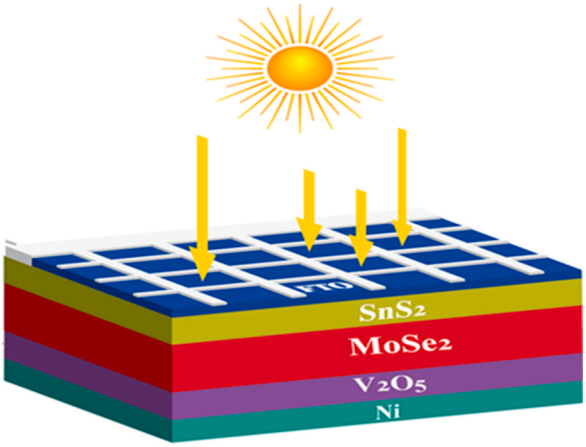

Fig. 16. The device structure of the optimized Ag/FTO/SnS_2/$MoSe_2$/V_2O_5/Ni cells.

Table 5
The Ag/FTO/ETL/$MoSe_2$/V_2O_5/Ni structures' output performance values are compared with those of earlier studies. (* = Optimum structure, E = Experimental, and T = Theoretical work).

Structure	Type of Work	V_{OC} (V)	J_{SC} (mA/cm^2)	FF (%)	PCE (%)	Ref.
FTO/In_2S_3/$MoSe_2$/V_2O_5	T	0.868957	42.5516	79.3968	29.3574	This work
FTO/ZnSe/$MoSe_2$/V_2O_5	T	0.918235	42.4789	78.6293	30.6699	This work
FTO/SnS_2/$MoSe_2$/V_2O_5	T	0.918005	42.5654	87.1994	34.0734	This work*
$MoSe_2$/Si	E	0.19	5.71	30.47	0.33	[77]
ZnO/ZnS/$MoSe_2$	T	0.8	22.19	–	17.51	[21]
$MoSe_2$/CIGS tandem SC	T	0.62	38.69	80.71	19.29	[23]
Mo/MoSe2/ZnO/FTO	T	0.822	29.22	85.67	20.58	[78]
Cu/FTO/CdS/MoSe2/Au	T	0.605	42.82	81.67	21.19	[44]
Al/FTO/ZnSe/MoSe2/MoSe2/Ni	T				23.75	[79]
Cu/FTO/CdS/MoSe2/CdTe/Au	T	0.747	43.57	83.09	27.05	[44]
Al/ITO/CdS/$MoSe_2$/In_2Te_3/Ni	T	1.10	31.06	87.28	29.94	[24]

4. Conclusions

Overall, this investigation presents a computational analysis (using SCAPS-1D) for 10 device arrangements involving the $MoSe_2$ absorber, SnS_2 ETL, and 7 different device configurations for HTL layers. The HTL is first optimized, focusing on the PV factors, in order to lessen the challenges of selecting the ideal device configuration. Three ETL devices based on In_2S_3, SnS_2, and ZnSe were available once HTL was optimized. Following modifications to the absorber layer thickness, acceptor and defect density, ETL thickness and donor density, and HTL acceptor along with defect density, a primary device (Ag/FTO/SnS_2/$MoSe_2$/V_2O_5/Ni) was chosen in light of its exceptional performance (PCE of 34.07 %, V_{OC} of 0.918 V, J_{SC} of 42.565 mAcm^{-2}, and FF of 87.19 %) in comparison to other device configurations under this study. Following device optimization, the effects of temperature, shunt and series resistance, recombination rate, charge carrier production, and other relevant factors have also been studied. The device with SnS_2 ETL performs better, as seen by the several device parameter adjustments, JV and QE characteristics curves with optimized results. In the near future, nevertheless, a portfolio based on the results of this numerical analysis may be used to produce eco-friendly SCs based on $MoSe_2$ absorber material.

Data availability

Data will be made available on reasonable request.

Ethical approval

All the authors declare that the manuscript does not have studies on human subjects, human data or tissue, or animals.

CRediT authorship contribution statement

Avijit Ghosh: Writing – review & editing, Writing – original draft, Visualization, Validation, Supervision, Software, Resources, Project administration, Methodology, Investigation, Funding acquisition, Formal analysis, Data curation, Conceptualization. **Abeer A. Hassan:** Writing – review & editing, Writing – original draft, Validation, Software, Formal analysis. **H.A. Alrafai:** Writing – review & editing, Writing – original draft, Validation, Software, Formal analysis. **Siham Khalaf Alla Abdelrahim:** Writing – review & editing, Writing – original draft, Validation, Software, Formal analysis.

Declaration of competing interest

The authors declare that they have no known competing financial interests or personal relationships that could have appeared to influence the work reported in this paper.

Acknowledgement

The authors extend their appreciation to the Deanship of Research and Graduate Studies at King Khalid University for funding this work through Large Research Project under grant number RGP2/94/45. The authors also would like to offer their heartfelt appreciation to Dr Marc Burgelman and his colleagues at the EIS Department at the University of Gent in Belgium for providing the opportunity to use the SCAPS-1D software.

References

[1] M.A. Matin, M. Dey, High performance ultra-thin CdTe solar cell with Lead Telluride BSF, in: 2014 International Conference on Informatics, Electronics & Vision (ICIEV), May 2014, pp. 1–5, https://doi.org/10.1109/ICIEV.2014.6850826.

[2] H. Yoon, et al., Rim2, a pyrimidine nucleotide exchanger, is needed for iron utilization in mitochondria, Biochem. J. 440 (1) (Nov. 2011) 137–146, https://doi.org/10.1042/BJ20111036.

[3] A.K. Patel, P.K. Rao, R. Mishra, S.K. Soni, Numerical study of a high-performance thin film CIGS solar cell with a-Si and MoTe2 hole transport layer, Optik 243 (Oct. 2021) 167498, https://doi.org/10.1016/j.ijleo.2021.167498.

[4] S. Hossain, M.M. Rahman, Solar energy prospects in Bangladesh: target and current status, Energy Power Eng. 13 (8) (2021) 322–332, https://doi.org/10.4236/epe.2021.138022.

[5] F. Perera, Pollution from Fossil-Fuel Combustion Is the Leading Environmental Threat to Global Pediatric Health and Equity : Solutions Exist, 2018, https://doi.org/10.3390/ijerph15010016.

[6] A.O.M. Maka, J.M. Alabid, Solar energy technology and its roles in sustainable development, Clean Energy 6 (3) (Jun. 2022) 476–483, https://doi.org/10.1093/ce/zkac023.

[7] K.L. Chopra, P.D. Paulson, V. Dutta, Thin-film solar cells: an overview, Prog. Photovoltaics Res. Appl. 12 (2–3) (Mar. 2004) 69–92, https://doi.org/10.1002/pip.541.

[8] T.D. Lee, A.U. Ebong, A review of thin film solar cell technologies and challenges, Renew. Sustain. Energy Rev. 70 (Apr. 2017) 1286–1297, https://doi.org/10.1016/j.rser.2016.12.028.

[9] M.A. Green, Y. Hishikawa, E.D. Dunlop, D.H. Levi, J. Hohl-Ebinger, A.W.Y. Ho-Baillie, Solar cell efficiency tables (version 52), Prog. Photovoltaics Res. Appl. 26 (7) (Jul. 2018) 427–436, https://doi.org/10.1002/pip.3040.

[10] M.F. Hossain, et al., Design and simulation numerically with performance enhancement of extremely efficient Sb2Se3-Based solar cell with V2O5 as the hole transport layer, using SCAPS-1D simulation program, Opt Commun. 559 (May 2024) 130410, https://doi.org/10.1016/j.optcom.2024.130410.

[11] M.F. Rahman, et al., The optical and electronic properties of inorganic halide perovskite Sr3NCl3 under applied biaxial strain, J. Mater. Sci. 58 (32) (Aug. 2023) 13100–13117, https://doi.org/10.1007/s10853-023-08825-5.

[12] M.A.B. Shanto, et al., Investigating how the electronic and optical properties of a novel cubic inorganic halide perovskite, Sr3NI3 are affected by strain, F1000Research 12 (Aug. 2023) 1005, https://doi.org/10.12688/f1000research.137044.1.

[13] A. Ghosh, et al., Structural, electronic and optical characteristics of inorganic cubic perovskite Sr 3 AsI 3, Opt. Contin. 2 (10) (Oct. 2023) 2144, https://doi.org/10.1364/OPTCON.495816.

[14] A. Ghosh, et al., Strain-induced changes in the electronic, optical and mechanical properties of the inorganic cubic halide perovskite Sr3PBr3 with FP-DFT, J. Phys. Chem. Solid. 191 (Aug. 2024) 112053, https://doi.org/10.1016/j.jpcs.2024.112053.

[15] M.F. Rahman, et al., Unraveling the strain-induced and spin–orbit coupling effect of novel inorganic halide perovskites of Ca3AsI3 using DFT, AIP Adv. 13 (8) (Aug. 2023), https://doi.org/10.1063/5.0156961.

[16] T. Böker, et al., Band structure of MoS_2 $MoSe_2$, Phys. Rev. B 64 (23) (Nov. 2001) 235305, https://doi.org/10.1103/PhysRevB.64.235305.

[17] A.R. Beal, J.C. Knights, W.Y. Liang, Transmission spectra of some transition metal dichalcogenides. I. Group IVA: octahedral coordination, J. Phys. C Solid State Phys. 5 (24) (Dec. 1972) 3531–3539, https://doi.org/10.1088/0022-3719/5/24/015.

[18] M. Moustafa, T. AlZoubi, Effect of the n-MoTe2 interfacial layer in cadmium telluride solar cells using SCAPS, Optik 170 (Oct. 2018) 101–105, https://doi.org/10.1016/j.ijleo.2018.05.112.

[19] S. Manzeli, D. Ovchinnikov, D. Pasquier, O.V. Yazyev, A. Kis, 2D transition metal dichalcogenides, Nat. Rev. Mater. 2 (8) (Jun. 2017) 17033, https://doi.org/10.1038/natrevmats.2017.33.

[20] M.Z. Iqbal, S. Alam, M.M. Faisal, S. Khan, Recent advancement in the performance of solar cells by incorporating transition metal dichalcogenides as counter electrode and photoabsorber, Int. J. Energy Res. 43 (8) (Jun. 2019) 3058–3079, https://doi.org/10.1002/er.4375.

[21] B. Zaidi, C. Shekhar, B. Hadjoudja, S. Gagui, B. Chouial, Optimization of highly efficient monolayer MoSe 2 based solar cells, Acta Phys. Pol., A 136 (3) (Sep. 2019) 495–497, https://doi.org/10.12693/APhysPolA.136.495.

[22] P. Tyagi, S. Choudhary, Modulating the optical and electrical properties of MoSe2 (Molybdenum diselenide) and WS2 (Tungsten disulfide) monolayer by the adsorption of halogen (F, Cl, Br, I and At) atoms, Opt. Quant. Electron. 54 (12) (Dec. 2022) 869, https://doi.org/10.1007/s11082-022-04271-w.

[23] B. Zaidi, C. Shekhar, B. Hadjoudja, S. Gagui, S. Zahra, M.A. Saeed, Simulation study of monolithic MoSe2/CIGS tandem solar cells, Discov. Mater. 1 (1) (Dec. 2021) 15, https://doi.org/10.1007/s43939-021-00016-w.

[24] B. Sultana, A.T.M.S. Islam, M.D. Haque, A. Kuddus, M.H. Ali, M.F. Rahman, Numerical study of MoSe 2 -based dual-heterojunction with in 2 Te 3 BSF layer toward high-efficiency photovoltaics, Phys. Scripta 98 (9) (Sep. 2023) 095935, https://doi.org/10.1088/1402-4896/acee29.

[25] P. De Sarkar, A. Paul, K.K. Ghosh, Thin film dichalcogenide MoSe2 solar cell with optimized design parameters, IOSR J. Electron. Commun. Eng. 12 (3) (Jul. 2017) 13–17, https://doi.org/10.9790/2834-1203041317.

[26] A. Jäger-Waldau, M. Lux-Steiner, E. Bucher, Thin films of MoSe2 and WSe2 prepared by soft selenization as bulk material for solar cells, in: E.C. Tenth (Ed.), Photovoltaic Solar Energy Conference, Springer Netherlands, Dordrecht, 1991, pp. 597–600, https://doi.org/10.1007/978-94-011-3622-8_153.

[27] Z. Chen, H. Liu, X. Chen, G. Chu, S. Chu, H. Zhang, Wafer-size and single-crystal MoSe 2 atomically thin films grown on GaN substrate for light emission and harvesting, ACS Appl. Mater. Interfaces 8 (31) (Aug. 2016) 20267–20273, https://doi.org/10.1021/acsami.6b04768.

[28] V. Manjunath, S. Bimli, P.A. Shaikh, S.B. Ogale, R.S. Devan, Understanding the role of inorganic carrier transport layer materials and interfaces in emerging perovskite solar cells, J. Mater. Chem. C 10 (42) (2022) 15725–15780, https://doi.org/10.1039/D2TC02911A.

[29] M.S. Reza, et al., Design and optimization of high-performance novel RbPbBr 3 -based solar cells with wide-band-gap S-chalcogenide electron transport layers (ETLs), ACS Omega (Apr. 2024), https://doi.org/10.1021/acsomega.3c08285.

[30] A. Ghosh, et al., Investigating of novel inorganic cubic perovskites of A3BX3 (A=Ca, Sr, B P, As, X=I, Br) and their photovoltaic performance with efficiency over 28, J. Alloys Compd. 986 (May 2024) 174097, https://doi.org/10.1016/j.jallcom.2024.174097.

[31] A. Ghosh, et al., Enhancing solar cell efficiency beyond 27% through the implementation of an efficient charge transport layer utilizing an innovative inorganic perovskite Sr3PI3, J. Phys. Chem. Solid. 190 (Jul. 2024) 112029, https://doi.org/10.1016/j.jpcs.2024.112029.

[32] S.H. Liu, J.R. Yuan, Y. Wu, X.H. Deng, Q.M. Yu, Numerical simulation of Sb2Se3-based solar cells, Chalcogenide Lett. 21 (3) (Mar. 2024) 229–241, https://doi.org/10.15251/CL.2024.213.229.

[33] T. Nusrat, T. Hasnat Ferdous, F. Tuz Zohra, Y. Arafat, Introducing various BSF materials and different doping concentrations in dual junction solar cell with a view to achieving optimal efficiency, in: 2018 IEEE International WIE Conference on Electrical and Computer Engineering (WIECON-ECE), Dec. 2018, pp. 110–113, https://doi.org/10.1109/WIECON-ECE.2018.8783095.

[34] M.K. Hossain, et al., An extensive study on charge transport layers to design and optimization of high-efficiency lead-free Cs2PtI6-based double-perovskite solar cells: a numerical simulation approach, Results Phys. 61 (Jun. 2024) 107751, https://doi.org/10.1016/j.rinp.2024.107751.

[35] M. Burgelman, K. Decock, S. Khelifi, A. Abass, Advanced electrical simulation of thin film solar cells, Thin Solid Films 535 (1) (2013) 296–301, https://doi.org/10.1016/j.tsf.2012.10.032.

[36] Y.H. Khattak, et al., Effect of CZTSe BSF and minority carrier life time on the efficiency enhancement of CZTS kesterite solar cell, Curr. Appl. Phys. 18 (6) (2018) 633–641, https://doi.org/10.1016/j.cap.2018.03.013.

[37] S. Sharbati, E. Norouzzadeh, S. Mohammadi, A simulation study to improve the efficiency of ZnO1-xSx/Cu2ZnSn (Sy, Se1-y)4 solar cells by composition-ratio control, Opt. Mater. 78 (2018) 259–265, https://doi.org/10.1016/j.optmat.2018.02.032.

[38] D. Sharma, R. Mehra, B. Raj, Mathematical Modelling and Simulation of CH3NH3Pb(I1-Xbrx)3 Based Perovskite Solar Cells for High Efficiency, 2021, https://doi.org/10.21203/rs.3.rs-1133949/v1.

[39] M.K. Hossain, et al., Numerical simulation and optimization of a CsPbI3-based perovskite solar cell to enhance the power conversion efficiency, New J. Chem. 47 (10) (2023) 4801–4817, https://doi.org/10.1039/d2nj06206b.

[40] M. Burgelman, P. Nollet, S. Degrave, Modelling polycrystalline semiconductor solar cells, Thin Solid Films 361–362 (Feb. 2000) 527–532, https://doi.org/10.1016/S0040-6090(99)00825-1.

[41] A. Ghosh, et al., A theoretical investigation of MoS2-based solar cells with CdS electron transport layer and V2O5 hole transport layer for boosting performance, Mater. Sci. Eng. B 307 (Sep. 2024) 117521, https://doi.org/10.1016/j.mseb.2024.117521.

[42] M.F. Rahman, et al., Design and numerical investigation of cadmium telluride (CdTe) and iron silicide (FeSi2) based double absorber solar cells to enhance power conversion efficiency, AIP Adv. 12 (10) (2022) 1–11, https://doi.org/10.1063/5.0108459.

[43] Mamta, K.K. Maurya, V.N. Singh, Influence of buffer layers on antimony selenide based solar cell, Opt. Mater. 126 (Apr. 2022) 112240, https://doi.org/10.1016/j.optmat.2022.112240.

[44] N. Rahman, et al., Impact of CdTe BSF layer on enhancing the efficiency of MoSe2 solar cell, J. Opt. (May 2024), https://doi.org/10.1007/s12596-024-01855-5.

[45] R. Kumari, M. Mamta, R. Kumar, Y. Singh, V.N. Singh, 24% efficient, simple ZnSe/Sb 2 Se 3 heterojunction solar cell: an analysis of PV characteristics and defects, ACS Omega 8 (1) (Jan. 2023) 1632–1642, https://doi.org/10.1021/acsomega.2c07211.

[46] I. Alam, M.A. Ashraf, Effect of different device parameters on tin-based perovskite solar cell coupled with in 2 S 3 electron transport layer and CuSCN and Spiro-OMeTAD alternative hole transport layers for high-efficiency performance, Energy Sources, Part A Recover. Util. Environ. Eff. 00 (00) (Sep. 2020) 1–17, https://doi.org/10.1080/15567036.2020.1820628.

[47] M.F. Rahman, et al., Exploring the impact of strain on the electronic and optical properties of inorganic novel cubic perovskite Sr 3 PI 3, Phys. Scripta 98 (11) (Nov. 2023) 115105, https://doi.org/10.1088/1402-4896/acfce9.

[48] M.A. Rahman, et al., Impact of A-cations modified on the structural, electronic, optical, mechanical, and solar cell performance of inorganic novel A 3 NCl 3 (A = Ba, Sr, and Ca) perovskites, Energy & Fuels (Apr. 2024), https://doi.org/10.1021/acs.energyfuels.4c00525.

[49] R.K. Yadav, et al., A qualitative study of SnSe thin film solar cells using SCAPS 1D and comparison with experimental results: a pathway towards 22.69% efficiency, Sol. Energy Mater. Sol. Cells 244 (Aug. 2022) 111835, https://doi.org/10.1016/j.solmat.2022.111835.

[50] M.H. Ali, M.A. Al Mamun, M.D. Haque, M.F. Rahman, M.K. Hossain, A. Z. Md Touhidul Islam, Performance enhancement of an MoS 2 -based heterojunction solar cell with an in 2 Te 3 back surface field: a numerical simulation approach, ACS Omega 8 (7) (Feb. 2023) 7017–7029, https://doi.org/10.1021/acsomega.2c07846.

[51] M. Al-Hattab, L. Moudou, M. Khenfouch, O. Bajjou, Y. Chrafih, K. Rahmani, Numerical simulation of a new heterostructure CIGS/GaSe solar cell system using SCAPS-1D software, Sol. Energy 227 (Oct. 2021) 13–22, https://doi.org/10.1016/j.solener.2021.08.084.

[52] F. Kherrat, et al., Performance enhancement of eco-friendly Cs3Sb2I9-based perovskite solar cell employing Nb2O5 and CuI as efficient charge transport layers, Micro and Nanostructures 183 (Nov. 2023) 207676, https://doi.org/10.1016/j.micrna.2023.207676.

[53] M. Mammeri, L. Dehimi, H. Bencherif, F. Pezzimenti, Paths towards high perovskite solar cells stability using machine learning techniques, Sol. Energy 249 (Jan. 2023) 651–660, https://doi.org/10.1016/j.solener.2022.12.002.

[54] S.R. Al Ahmed, A. Sunny, S. Rahman, Performance enhancement of Sb2Se3 solar cell using a back surface field layer: a numerical simulation approach, Sol. Energy Mater. Sol. Cells 221 (Mar. 2021) 110919, https://doi.org/10.1016/j.solmat.2020.110919.

[55] M.S. Reza, et al., Boosting efficiency above 28% using effective charge transport layer with Sr 3 SbI 3 based novel inorganic perovskite, RSC Adv. 13 (45) (2023) 31330–31345, https://doi.org/10.1039/D3RA06137J.

[56] R. Jeyakumar, A. Bag, R. Nekovei, R. Radhakrishnan, Influence of electron transport layer (TiO2) thickness and its doping density on the performance of CH3NH3PbI3-based planar perovskite solar cells, J. Electron. Mater. 49 (6) (Jun. 2020) 3533–3539, https://doi.org/10.1007/s11664-020-08041-w.

[57] N. Jahan, et al., A comparative study of CuO based solar cell with ZnTe HTL and SnS2 ETL using SCAPS 1D simulation, J. Opt. (Apr. 2024), https://doi.org/10.1007/s12596-024-01800-6.

[58] Z. Gu, et al., Novel planar heterostructure perovskite solar cells with CdS nanorods array as electron transport layer, Sol. Energy Mater. Sol. Cells 140 (Sep. 2015) 396–404, https://doi.org/10.1016/j.solmat.2015.04.015.

[59] C. Chen, et al., Characterization of basic physical properties of Sb2Se3 and its relevance for photovoltaics, Front. Optoelectron. 10 (1) (Mar. 2017) 18–30, https://doi.org/10.1007/s12200-017-0702-z.

[60] M. Burgelman, J. Verschraegen, S. Degrave, P. Nollet, Modeling thin-film PV devices, Prog. Photovoltaics Res. Appl. 12 (23) (Mar. 2004) 143–153, https://doi.org/10.1002/pip.524.

[61] H. Zhang, S. Cheng, J. Yu, H. Zhou, H. Jia, Prospects of Zn(O,S) as an alternative buffer layer for Cu 2 ZnSnS 4 thin-film solar cells from numerical simulation, Micro & Nano Lett. 11 (7) (Jul. 2016) 386–390, https://doi.org/10.1049/mnl.2016.0130.

[62] Y.H. Khattak, F. Baig, H. Toura, S. Beg, B.M. Soucase, Efficiency enhancement of Cu2BaSnS4 experimental thin-film solar cell by device modeling, J. Mater. Sci. 54 (24) (Dec. 2019) 14787–14796, https://doi.org/10.1007/s10853-019-03942-6.

[63] O. Ahmad, A. Rashid, M.W. Ahmed, M.F. Nasir, I. Qasim, Performance evaluation of Au/p-CdTe/Cs2TiI6/n-TiO2/ITO solar cell using SCAPS-1D, Opt. Mater. 117 (Jul. 2021) 111105, https://doi.org/10.1016/j.optmat.2021.111105.

[64] Y. Zhou, A. Gray-Weale, A numerical model for charge transport and energy conversion of perovskite solar cells, Phys. Chem. Chem. Phys. 18 (6) (2016) 4476–4486, https://doi.org/10.1039/C5CP05371D.

[65] A. Ghosh, et al., Inorganic novel cubic halide perovskite Sr3AsI3: strain-activated electronic and optical properties, Heliyon 9 (8) (Aug. 2023) e19271, https://doi.org/10.1016/j.heliyon.2023.e19271.

[66] M.F. Rahman, et al., First-principles analysis of how Cobalt doping affects the structural, electronic, and optical properties of α-MoO3, Indian J. Phys. (Dec. 2023), https://doi.org/10.1007/s12648-023-03043-w.

[67] M.F. Rahman, et al., An investigation on strain-incited electronic and optical properties of novel inorganic cubic material Sr3AsCl3, J. Solid State Chem. 328 (Dec. 2023) 124341, https://doi.org/10.1016/j.jssc.2023.124341.

[68] F. Behrouznejad, S. Shahbazi, N. Taghavinia, H.-P. Wu, E. Wei-Guang Diau, A study on utilizing different metals as the back contact of CH 3 NH 3 PbI 3 perovskite solar cells, J. Mater. Chem. A 4 (35) (2016) 13488–13498, https://doi.org/10.1039/C6TA05938D.

[69] M.S. Reza, et al., New highly efficient perovskite solar cell with power conversion efficiency of 31% based on Ca3NI3 and an effective charge transport layer, Opt Commun. 561 (Jun. 2024) 130511, https://doi.org/10.1016/j.optcom.2024.130511.

[70] H. Heriche, Z. Rouabah, N. Bouarissa, New ultra thin CIGS structure solar cells using SCAPS simulation program, Int. J. Hydrogen Energy 42 (15) (Apr. 2017) 9524–9532, https://doi.org/10.1016/j.ijhydene.2017.02.099.

[71] E. Karimi, S.M.B. Ghorashi, Simulation of perovskite solar cell with P 3 HT hole-transporting materials, J. Nanophotonics 11 (3) (Mar. 2017) 032510, https://doi.org/10.1117/1.JNP.11.032510.

[72] M.S. Islam, et al., Investigation strain effects on the electronic, optical, and output performance of the novel inorganic halide perovskite Sr3SbI3 solar cell, Chin. J. Phys. 88 (Apr. 2024) 270–286, https://doi.org/10.1016/j.cjph.2024.01.011.

[73] M.F.I. Buian, et al., A novel investigation into strain-induced changes in the physical properties and solar cell performances of lead-free Ca3NCl3 perovskite, Mater. Sci. Semicond. Process. 180 (Sep. 2024) 108580, https://doi.org/10.1016/j.mssp.2024.108580.

[74] A. Ghosh, et al., Improving the power conversion efficiency of RbPbBr3 absorber based solar cells through the variation of efficient hole transport layers, J. Phys. Chem. Solid. 193 (2024) 112179, https://doi.org/10.1016/j.jpcs.2024.112179. Oct.

[75] M.S. Islam, et al., An in-depth analysis of how strain impacts the electronic, optical, and output performance of the Ca3NI3 novel inorganic halide perovskite, J. Phys. Chem. Solid. 185 (Feb. 2024) 111791, https://doi.org/10.1016/j.jpcs.2023.111791.

[76] P. Khan, T. Mahmood, K. Ayub, S. Tabassum, M. Amjad Gilani, Turning diamondoids into nonlinear optical materials by alkali metal Substitution: a DFT investigation, Opt Laser. Technol. 142 (2021) 107231–Oct, https://doi.org/10.1016/j.optlastec.2021.107231.

[77] J. Yuan, Z. Ai, M. Yu, R. Huang, Q. Cheng, Growth and application of MoSe 2 in solar cells, Int. J. Mod. Phys. B 36 (25) (Oct. 2022), https://doi.org/10.1142/S0217979222501685.
[78] T.A. Chowdhury, R.B. Arif, H. Israq, N. Sharmili, R.S. Shuvo, SCAPS numerical design of MoSe2 solar cell for different buffer layers, Chalcogenide Lett. 21 (2) (Mar. 2024) 175–187, https://doi.org/10.15251/CL.2024.212.175.
[79] M.N. Sarder, M.A. Al Mamun, M.H. Ali, M.D. Haque, M.F. Rahman, A.Z.M.T. Islam, Numerical simulation of MoSe2 based solar cell by SCAPS-1D, in: 2022 International Conference on Recent Progresses in Science, Engineering and Technology (ICRPSET), Dec. 2022, pp. 1–5, https://doi.org/10.1109/ICRPSET57982.2022.10188504.